

Optimized tandem catalyst patterning for CO₂ reduction flow reactors

Jack Guo^{a,*}, Thomas Roy^a, Nitish Govindarajan^b, Joel B. Varley^b, Jonathan Raison^{c,e}, Jinyoung Lee^{c,d,f}, Jiwook Jang^{f,g}, Dong Un Lee^{c,d}, Thomas F. Jaramillo^{c,d}, Tiras Y. Lin^{a,*}

^a*Computational Engineering Division, Lawrence Livermore National Laboratory, Livermore, CA 94550, USA*

^b*Materials Science Division, Lawrence Livermore National Laboratory, Livermore, CA 94550, USA*

^c*SUNCAT Center for Interface Science and Catalysis, Department of Chemical Engineering, Stanford University, Stanford, CA 94305, USA*

^d*SUNCAT Center for Interface Science and Catalysis, SLAC National Accelerator Laboratory, Menlo Park, CA 94025, USA*

^e*TotalEnergies Research & Technology USA LLC, Houston, TX 77002, USA*

^f*School of Energy and Chemical Engineering, Ulsan National Institute of Science and Technology (UNIST), Ulsan, Republic of Korea*

^g*Graduate School of Carbon Neutrality, Ulsan National Institute of Science and Technology (UNIST), Ulsan, Republic of Korea*

Abstract

Tandem catalysis involves two or more catalysts arranged in proximity within a single reaction vessel. Each catalyst prefers different reaction pathways and products, and so the tandem design synergistically seeks to leverage the strengths of each and maximize overall system performance and efficiency. This study presents the integration of continuum transport modeling with design optimization in a simplified two-dimensional flow reactor setup for electrochemical CO₂ reduction, as a proof of concept towards constructing an optimization-based reactor design framework. Ag catalysts provide the CO₂ \longrightarrow CO reaction capability, and Cu catalysts provide the CO \longrightarrow high-value products reaction capability. Given a set of input parameters – applied surface voltage, electrolyte flow rate, and number of catalyst sections – the optimization algorithm uses adjoint methods to modify the Ag/Cu surface patterning in order to maximize the current density toward high-value products, such as ethylene. The optimized designs, which strongly depend on these input parameters, yield significant performance enhancement especially at more negative applied voltages (i.e., stronger surface reactions) and for larger numbers of patterning sections. For an applied voltage of -1.7 V vs. SHE, the 12-section optimized design increases the current density towards ethylene by up to 65% compared to the unoptimized 2-section design. Observed differences in the production and consumption of CO (the key intermediate species) provide insight into increased

ethylene production in the optimized cases. The concentration fields highlight how optimized patterns minimize zones of low reactant concentration on the catalyst surface to increase production of high-value further-reduced products.

Keywords:

CO₂ reduction, design optimization, tandem catalysis, mass transport, flow reactor

1. Introduction

The electrochemical reduction of CO₂ (CO₂R) into higher-value products is an emerging and promising method used in the global shift towards a sustainable energy and chemical economy. Converting CO₂ into useful fuels and high-value chemicals directly removes a harmful greenhouse gas from the atmosphere. As an added benefit, powering the electrochemical CO₂R process using a renewable energy source provides a sustainable pathway to achieve chemical processing and energy storage while mitigating additional greenhouse gas emissions.

While CO₂ electrolyzers have made significant strides as a technology¹, further progress is needed to achieve performance at commercial-scale and cost-effective levels. Copper-based catalysts are of interest due to their unique ability to produce high-value hydrocarbons, aldehydes, and alcohols in substantial amounts (Faradaic efficiencies)². However, electrolyzers using copper catalysts suffer from high overpotential (low energy efficiencies) at desired current densities and limited selectivity towards the desired high-value products. Issues known to contribute to this limited performance include local reaction environment features that promote hydrogen evolution reaction (HER)³ and other unwanted side reactions, limited CO₂ availability at the catalyst surface⁴, and ineffective management of intermediate species transport⁵. Further investigation into these (and more) physical phenomena is needed towards designing high-performance CO₂R electrolyzers. To this end, computational simulations have emerged as a powerful tool for investigating the high complexity of the underlying physicochemical processes and the wide landscape of reactor designs found in CO₂ electrolysis. Simulation capabilities that use continuum modeling focus on the larger-scale behavior

*Corresponding author

Email addresses: guo9@11nl.gov (Jack Guo), lin46@11nl.gov (Tiras Y. Lin)

while representing the atomistic-scale information with an appropriate low-order description (such as using Butler-Volmer equations to model the kinetics). Such continuum modeling simulations have emerged as a set of powerful tools in recent years and have demonstrated the ability to provide insight into relevant electrolyzer factors, including the aforementioned issues connected with performance degradation. Notably, previous studies have provided information on the interactions between mass/ion transport, fluid flow, reaction kinetics^{6,7}, key design parameters such as porosity and catalyst loading⁸, and structural details of the electrical double layer⁹. Understanding these factors is important for describing selectivity and activity relationships in CO₂ electrolysis, particularly in custom reactor design architectures.

In electrolyzers, the previously mentioned ineffective management of intermediate species transport presents itself through a range of symptoms, including excess intermediate species that are advected away before being utilized^{5,10} and as diffusion/mixing-caused losses for large spacings between electrodes¹¹. Specifically for CO₂R reaction pathways on copper, carbon monoxide (CO) is the crucial intermediate species for the production of further reduced high-value products (i.e., requiring $> 2e^-$ transfers)². To address these transport limitations for intermediate species, designs that utilize multiple catalysts in proximity to synergistically leverage the reaction strengths of each catalyst material have attracted recent research attention^{12,13,14,15}. In such designs, one catalyst is effective at converting a given reactant species to an intermediate species, and a second catalyst is effective at converting the intermediate species to the desired end product(s). With the catalysts placed in proximity, the intermediate species is transported directly from the first to the second catalyst without the need for intermediate isolation or other specialized processing steps. The reduced travel distance of the intermediate species, compared to that of traditional reactor designs, results in increased residence time and availability of the intermediate species near the second catalyst (i.e., CO near the Cu catalyst for CO₂R⁵), allowing for increased utilization that results in higher production and selectivity towards desired products than achieved by a single catalyst setup. This described approach to catalyst patterning is known as tandem catalysis, which is how it shall be referred to in this paper. Note that in other published studies, the approach has also been referred to as cascade, sequential, domino, spillover, or sequential cascade catalysis. For CO₂R, the prod-

uct distribution for polycrystalline metal electrode catalysts was first comprehensively quantified in studies by Hori et al.^{16,17,18,19,20} using an electrolysis cell with CO₂-saturated 0.1 M KHCO₃ electrolyte at 5.0 mA/cm². These studies established that Au, Ag, Zn, Fe, and Ga catalysts primarily produce CO; notably, Au and Ag perform especially well, boasting Faradaic efficiency values towards CO of > 80%. The majority of the other tested metal catalysts are categorized as either mainly producing formate (HCOO⁻) or mainly reducing water to hydrogen (H₂). Distinctively, Cu is unique in its ability to produce high-value products, including C₂₊ products, at appreciable Faradaic efficiencies. Given the rationale and goals of tandem catalysis described previously, in CO₂R it is thus sensible to choose Au or Ag as the first catalyst (to perform CO₂ → CO) and Cu as the second catalyst (to perform CO → desired high-value final products including ethylene and ethanol). Therefore, this combination of Au/Ag + Cu catalysts has been utilized in numerous tandem catalyst studies, covering both experimental and computational approaches, in the CO₂R literature. The catalysts setups of these studies span a range of different designs, including interspersed spheres/particles^{21,22}, alternating planar sections^{11,12}, dots on planar sheets¹², particles interspersed within a bed of needles¹⁰, nanoparticles on a reactive flat substrate²³, and segmented catalyst layers of a gas diffusion electrode (GDE)⁵, among others. These studies and the overall body of work have provided key preliminary insight into the electrochemical behaviors and the effective design principles for tandem catalysis applied to CO₂R electrolyzers.

Thus far, CO₂R tandem catalysis studies have been primarily limited to *forward analysis*: a specific setup or patterning of catalysts is proposed and evaluated in an electrolyzer setting (either experimentally or through simulations), but the resulting insights are not directly used to update or improve the design. In contrast, *design optimization* methods^{24,25} offer a systematic framework for exploring the electrolyzer design space and improving performance. By exploiting the sensitivity of the performance metric to the catalyst patterning, the design can be iteratively refined and the problem re-solved until reaching an optimal configuration. A natural formulation of this approach is as a PDE-constrained optimization problem, in which the governing transport and reaction equations act as constraints while the catalyst patterning serves as the design variable. Such methods have been applied in a number of applications, including shape/topology optimiza-

tion for aerospace structural design²⁶, multi-body robotics systems²⁷, and even electrochemical systems^{28,29,30,31}. However, the use of design optimization in electrochemical systems remains relatively nascent, presenting a significant opportunity to leverage these techniques to guide the spatial arrangement of catalysts for enhanced CO₂R performance.

The study presented in this paper combines the capabilities of 1) computational simulations with continuum transport modeling and 2) design optimization, within a simplified case study of tandem catalysis for CO₂R. Our setup involves a two-dimensional (2D) flow cell plane reactor setup with Ag and Cu electrode catalyst surfaces. The procedures, performance metrics, and concentration flow fields are presented for designs that optimize the output of desired products across a sweep of various relevant input parameters: electrode applied voltage, electrolyte flow rate, and degree of patterning (the total number of Ag/Cu catalyst sections). It is demonstrated that the optimal patterning design strongly depends on each of these input parameters. Noticeable improvements in the current density towards desired products such as ethylene can be achieved, especially at more negative applied voltages and by using high patterning frequencies (i.e., a large number of Ag/Cu sections).

The results from this study provide general insight into optimal reactor design and concentration field behavior for tandem catalyst setups. However, realistic, industrially-relevant CO₂R designs include complicated and sophisticated components, such as gas diffusion electrodes (GDEs), whose effects are not fully captured by our current setup. Nevertheless, this study is intended to provide a proof-of-concept and first step towards optimization of more realistic electrolyzer geometries.

The remainder of the paper is organized as follows. Section 2 presents the formulation of the problem as well as the computational details of the governing equations (for the chemistry, species transport, and fluid) and of the optimization methodology. Section 3 shows the results of the study and associated discussion. Finally, section 4 provides conclusions and thoughts regarding future directions of work.

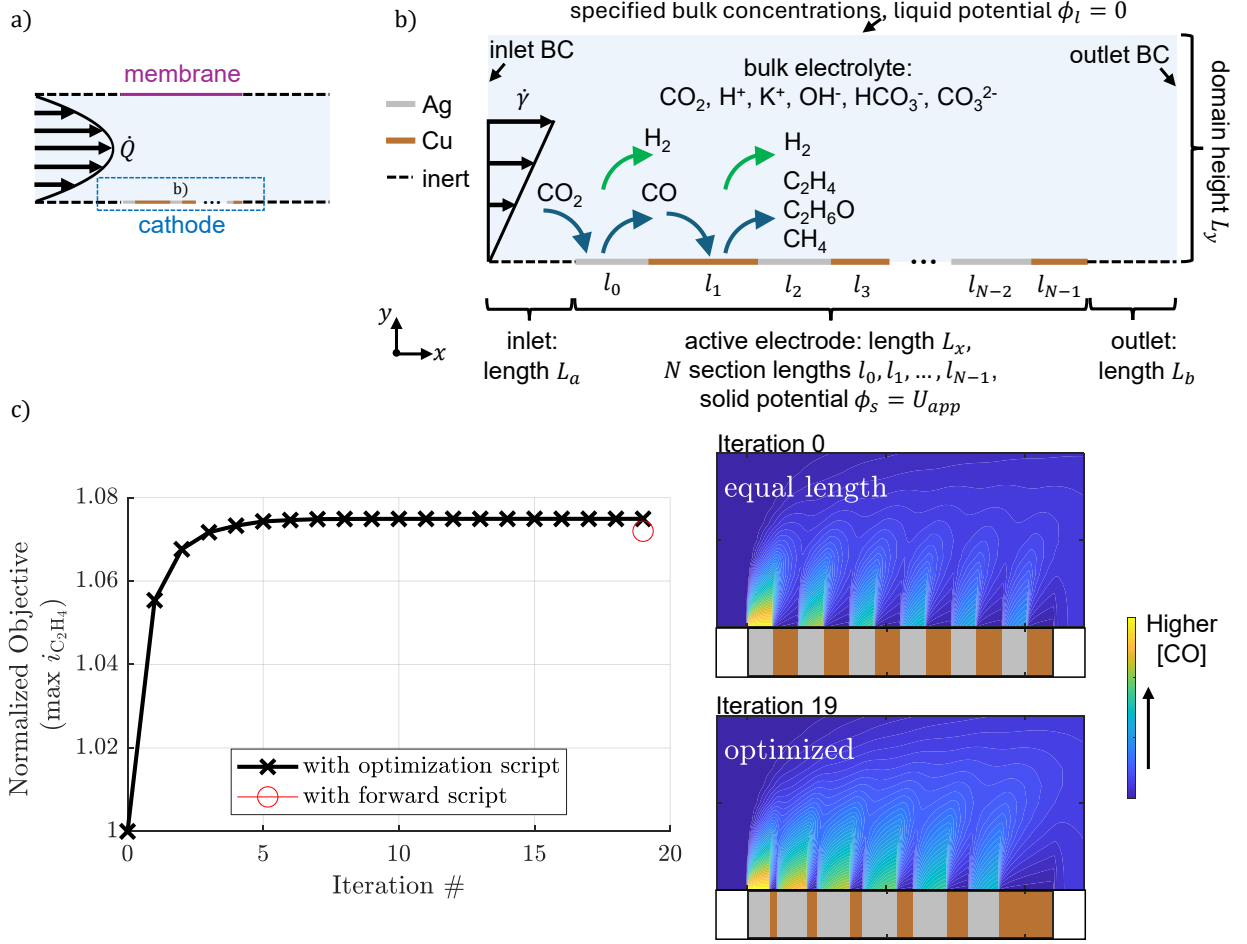


Figure 1: a) Schematic of a general flow reactor configuration, where \dot{Q} is the volumetric flow rate flowing between two flat plates. We focus on the mass transfer phenomena near the cathode, as highlighted in panel b. b) Schematic of computational simulation setup, with a shear flow of aqueous electrolyte solution flowing over the cathode portion and the inlet/outlet regions. c) Plot of the normalized objective function – the maximum ethylene current density, calculated per eq. (25) – for each optimization iteration step number, for an example optimization case (parameters: $N = 12$, flow rate = 3.0 ml/min, $U_{app} = -1.7$ V vs. SHE). The Ag/Cu section lengths and example CO concentration fields for the (initial) equal length pattern at iteration 0 and for the final optimized pattern at iteration 19 are shown.

2. System description and methodology

2.1. Domain setup and problem formulation

Figure 1 provides a schematic overview of the setup used in this work. Figure 1a shows a diagram of an example flow reactor half cell. Liquid electrolyte is flowed in between the cathode and the membrane with a parabolic velocity profile (for plane Poiseuille flow) at a prescribed volumetric flow rate.

Local features such as the local CO_2 and CO concentrations, pH, and boundary layer effects are critical ingredients that determine the yields of the desired products in the reactor system; thus, the computational setup was designed with the focused study of such features in mind. Figure 1b shows the computational simulation domain used in this work, which comprises the zoomed-in region near the cathode of the half cell in fig. 1a. The domain is modeled as a two-dimensional (2D) region. The fluid behavior near the electrolyte/electrode interface is well-approximated as a shear flow with shear rate $\dot{\gamma}$, as is discussed in further detail in section 2.3.

In the bulk region above the interface (for $0 < y < L_y$), an aqueous electrolyte solution flows in at the inlet, consisting of 500 mM KHCO_3 and 34 mM CO_2 . A number of species – CO_2 , H^+ , OH^- , HCO_3^- , and CO_3^{2-} – participate in the bicarbonate bulk reactions and are also transported throughout the bulk region. K^+ does not participate in the bulk reactions but is still present in the bulk and so must be treated as a transported species. Details of the bulk electrolyte reactions and transport governing equations are provided in section 2.2.1.

The solid surface of the computational domain (at $y = 0$) consists of an active electrode region with length L_x , which is located in between two inert (non-reactive) portions that serve to minimize the computational boundary effects and to better capture the large fluxes at the beginning and end of the electrode. The inert portions consist of a leading inlet with length L_a and a trailing outlet with length L_b . For this study, $L_x = 1.1$ cm, and $L_a = L_b = L_x/10$. As discussed in section 2.3, the example 3D flow channel that this study is based on has a length of 2.2 cm. To yield a computationally manageable case, the length was reduced by 50% for the value of L_x . For a given total number of sections N (an input parameter of the system), the active electrode region is comprised of N Ag/Cu sections, with the patterning determined by the section lengths l_j for

$j = 0, 1, \dots, N - 1$. Figure 1b also schematically shows the reactions included in the setup. The Ag section features a $\text{CO}_2 \longrightarrow \text{CO}$ surface reaction, and the Cu section surface chemistry include $\text{CO} \longrightarrow \text{C}_2\text{H}_4$, $\text{CO} \longrightarrow \text{C}_2\text{H}_6\text{O}$, and $\text{CO} \longrightarrow \text{CH}_4$ surface reactions. Both Ag and Cu sections also include the hydrogen evolution reaction to produce H_2 . Details of the electrochemical surface reaction model formulation are provided in section 2.2.2 and section 2.2.3. We stress that CO is not included in the input electrolyte stream, and so for this study’s setup, any CO in the system must be generated as a product by the Ag sections and is then used as a reactant by the Cu sections. These species that have been newly introduced by the surface reactions do not participate in the bulk reactions, but their transport within the bulk region is still modeled, as is discussed in section 2.2.1. To make use of the cascade/tandem nature of the electrode surface reactions, the patterns in this study consist of repeating pairs of Ag and Cu sections: Ag, Cu, Ag, Cu, ..., Ag, Cu; with this choice, only even values of N are considered.

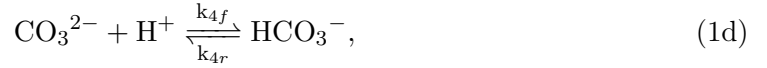
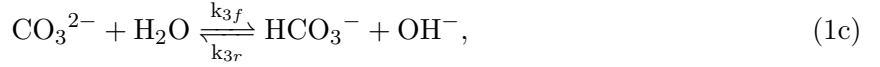
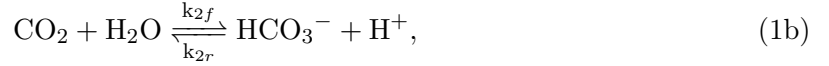
The boundary conditions for the system are also schematically listed in fig. 1b; these are explained in detail in section 2.2.1, section 2.2.2, and section 2.2.3.

Figure 1c shows an optimization case at an example set of conditions. The objective function, chosen to be the maximum ethylene current density as calculated per eq. (25), is plotted and is shown to be maximized as the optimization algorithm modifies the section lengths l_j with each successive iteration step until convergence. The beginning and end patterns, with the corresponding example CO concentration fields, are also shown. The initial pattern configuration is set as equal section lengths for all sections (Ag and Cu), while the final optimized pattern configuration (at iteration step 19) is a nontrivial configuration with varied section lengths. Analysis and discussion of the equal length case versus optimized case, for this set of conditions and for other conditions, are provided in section 3. Details of the optimization methodology are described in section 2.4. Note that in the objective vs. iteration # plot, the value of the normalized objective obtained from the optimization script is plotted for each iteration step. Additionally, the normalized objective value obtained from the forward script (which is treated as the true objective function value) is also plotted for the final iteration step and has a slightly different value. This detail is a consequence of the optimization procedures and is also explained in section 2.4.

2.2. Governing equations

2.2.1. Bulk (bicarbonate electrolyte) reactions and transport

The following set of governing reactions describes the buffer chemistry occurring in the bulk bicarbonate electrolyte³²:



k_{jf} and k_{jr} are the forward and reverse reaction rates, respectively, for reaction j . The steady equilibrium Nernst-Planck (NP) equations describe the species transport. For the N_{species} total species, the equation for each species k is written as

$$0 = -\nabla \cdot \mathbf{J}_k + \sum_j R_{j,k}, \quad (2)$$

where the reaction term $R_{j,k}$ for reaction j and species k is defined as

$$R_{j,k} = s_{k,j} c_{ref} \left(k_{jf} \prod_{m, s_{m,j} < 0} a_m^{-s_{m,j}} - k_{jr} \prod_{m, s_{m,j} > 0} a_m^{s_{m,j}} \right), \quad (3)$$

where $s_{k,j}$ is the stoichiometric coefficient and $a_m = c_m/c_{ref}$ is the activity of species m given concentration c_m and reference concentration $c_{ref} = 1\text{M}$. \mathbf{J}_k is the flux of species k , defined as

$$\mathbf{J}_k = -D_k \nabla c_k - z_k u_k F c_k \nabla \phi_l + \mathbf{v} c_k. \quad (4)$$

For species k , c_k represents the concentration, D_k is the diffusivity, z_k is the valency, and u_k is the ionic mobility, given from the Nernst-Einstein relation and written as

$$u_k = \frac{D_k}{RT}, \quad (5)$$

where R is the universal gas constant and T is the thermodynamic temperature. F is Faraday's constant, ϕ_l is the fluid (electrolyte) potential, and \mathbf{v} is the fluid (electrolyte) flow velocity. \mathbf{v} is modeled as a simple shear flow with shear rate $\dot{\gamma}$,

$$\mathbf{v} = \begin{bmatrix} \dot{\gamma}y \\ 0 \end{bmatrix}, \quad (6)$$

as discussed in more detail in section 2.3. Section S1 of the Supplementary Information document provides the tabulated diffusivity values (in table S1) and reaction rate constant values (in table S2).

These N_{species} transport equations are used to solve for $N_{\text{species}} + 1$ unknown variables (N_{species} concentrations $c_1, c_2, \dots, c_{N_{\text{species}}}$ in addition to the fluid potential ϕ_l). The additional equation needed to complete the system is the electroneutrality approximation:

$$\sum_k z_k c_k = 0. \quad (7)$$

Boundary conditions. The following boundary conditions are used:

1. Bottom of domain ($y = 0$): catalyst surface chemistry; this provides boundary conditions for the ionic current \mathbf{i}_2 ,

$$\mathbf{i}_2 \cdot \mathbf{n} = - \sum_p i_{\text{p,local}}, \quad (8)$$

and for the mass flux \mathbf{N}_k for species k ,

$$\mathbf{N}_k \cdot \mathbf{n} = - \sum_p \frac{s_{k,p} i_{\text{p,local}}}{n_p F}, \quad (9)$$

where n represents the number of electrons transferred and p is the index for each charge-transfer reaction in the system. The Tafel expressions for $i_{p,\text{local}}$ are provided in section 2.2.2 and section 2.2.3. For the inert inlet and outlet regions, $\mathbf{i}_2 \cdot \mathbf{n} = \mathbf{N}_k \cdot \mathbf{n} = 0$.

2. Top of domain ($y = L_y$):

- (a) $\phi_l = 0$
- (b) $c_{\text{CO}_2} = 34 \text{ mM}$ (from Henry's constant at a pressure of 1 atmosphere)
- (c) $c_{\text{K}^+} = 500 \text{ mM}$ in this study; then, c_{OH^-} , $c_{\text{HCO}_3^-}$, $c_{\text{CO}_3^{2-}}$, c_{H^+} are determined at chemical equilibrium from the bulk reactions provided in eq. (1)
- (d) $c_{\text{CO}} = c_{\text{H}_2} = c_{\text{CH}_4} = c_{\text{C}_2\text{H}_4} = c_{\text{C}_2\text{H}_6\text{O}} = 0$

3. Inlet: $\mathbf{J}_k \cdot \mathbf{n} = c_{k,\text{bulk}} \mathbf{v} \cdot \mathbf{n}$

4. Outlet: $\mathbf{J}_k \cdot \mathbf{n} = c_k \mathbf{v} \cdot \mathbf{n}$

Here, \mathbf{J}_k is the flux and $c_{k,\text{bulk}}$ is the bulk concentration of species k , and \mathbf{n} is the unit outward normal vector.

2.2.2. Surface (Ag catalyst) chemistry

The surface chemistry on the Ag catalytic surface is governed by the following reactions:



The Tafel expressions³³ to model this surface chemistry in eq. (10) and eq. (11) are given as the following:

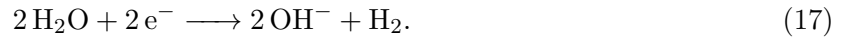
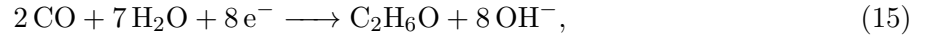
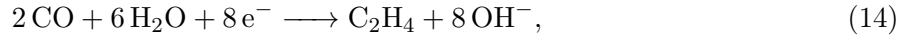
$$i_{\text{CO},\text{local}} = \left(\frac{a_{\text{CO}_2}}{a_{\text{CO}_2}^{\text{bulk}}} \right)^{-\gamma_{\text{CO}_2,\text{CO}}} \left(\frac{a_{\text{OH}^-}}{a_{\text{OH}^-}^{\text{bulk}}} \right)^{-\gamma_{\text{OH}^-,\text{CO}}} i_{0,\text{CO}} \left(-\exp \left[-\frac{\alpha_{c,\text{CO}} F}{RT} \eta_{s,\text{CO}} \right] \right), \quad (12)$$

$$i_{\text{H}_2,\text{local}} = \left(\frac{a_{\text{OH}^-}}{a_{\text{OH}^-}^{\text{bulk}}} \right)^{-\gamma_{\text{OH}^-,\text{H}_2}} i_{0,\text{H}_2} \left(-\exp \left[-\frac{\alpha_{c,\text{H}_2} F}{RT} \eta_{s,\text{H}_2} \right] \right). \quad (13)$$

The parameters (definitions and values) and validation of the implementation are provided in sections S3 and S4 of the Supplementary Information document.

2.2.3. Surface (Cu catalyst) chemistry

The surface chemistry on the Cu catalytic surface is governed by the following reactions:



These Tafel expression formulations³⁴ to model this surface chemistry in equations eq. (14) through eq. (17) are given as the following:

$$i_{\text{C}_2\text{H}_4, \text{local}} = \left(\frac{c_{\text{CO}}}{c_{\text{ref}}} \right) i_{0, \text{C}_2\text{H}_4} \left(- \exp \left[- \frac{\alpha_{c, \text{C}_2\text{H}_4} F}{RT} \eta_{s, \text{C}_2\text{H}_4} \right] \right), \quad (18)$$

$$i_{\text{C}_2\text{H}_6\text{O}, \text{local}} = \left(\frac{c_{\text{CO}}}{c_{\text{ref}}} \right) i_{0, \text{C}_2\text{H}_6\text{O}} \left(- \exp \left[- \frac{\alpha_{c, \text{C}_2\text{H}_6\text{O}} F}{RT} \eta_{s, \text{C}_2\text{H}_6\text{O}} \right] \right), \quad (19)$$

$$i_{\text{CH}_4, \text{local}} = \left(\frac{c_{\text{CO}}}{c_{\text{ref}}} \right) i_{0, \text{CH}_4} \left(- \exp \left[- \frac{\alpha_{c, \text{CH}_4} F}{RT} \eta_{s, \text{CH}_4} \right] \right), \quad (20)$$

$$i_{\text{H}_2, \text{local}} = i_{0, \text{H}_2} \left(-\exp \left[-\frac{\alpha_{c, \text{H}_2} F}{RT} \eta_{s, \text{H}_2} \right] \right). \quad (21)$$

The parameters (definitions and values) and validation of the implementation are provided in sections S5 and S6 of the Supplementary Information document.

An assumption for simplicity utilized in this study is that the $\text{CO}_2 \longrightarrow \text{CO}$ capability on Cu is omitted. The justification for this choice arises from the following arguments:

1. Except at less negative applied voltages ($U_{app} \gtrsim -1.2$ V vs. SHE), the CO current density values on Ag (using the model parameters in this study³³) are significantly larger than published values of the CO net current density values on Cu³⁵. More quantitatively, the reported net Cu $i_{\text{CO}, \text{local}}$ values do not exceed $\simeq 0.2$ mA/cm², while the Ag $i_{\text{CO}, \text{local}}$ modeled values in this study's voltage range span $\simeq 1.5$ to 5 mA/cm².
2. As observed in the CO₂R on Cu literature³⁵, the current densities of H₂, C₂H₄, C₂H₆O are larger than the CO net current density in the range of applied voltages considered in this study. CH₄ values are comparable to the CO net values at less negative applied voltages but quickly become much larger moving towards more negative applied voltages. More quantitatively, at more negative applied voltages, the H₂, C₂H₄, and CH₄ current density values are at least 10 \times as large and the C₂H₆O current density values are $\simeq 5 - 10\times$ as large as the net CO current density values.
3. It is difficult, experimentally, to obtain accurate $\text{CO}_2 \longrightarrow \text{CO}$ kinetics data on Cu that is not compromised by CO₂ mass transport limitations. It is thus a challenge to obtain reliable Tafel parameters to be used for computational modeling. Previous modeling studies have typically turned to simplified model representations of the Cu CO₂R kinetics, such as assuming a single-step 6-electron electrochemical reaction³⁶ which focuses on capturing trends from modifications to the input parameters.

If the $\text{CO}_2 \longrightarrow \text{CO}$ kinetics on Cu capability were to be included and considered, it is anticipated that the optimized designs would favor longer Cu section lengths than are obtained with this study's

setup; however, the qualitative takeaway messages from the design trends should still hold.

2.3. Fluid flow setup

The fluid flow velocity \mathbf{v} is modeled as a shear flow with shear rate $\dot{\gamma}$, per eq. (6). The value of $\dot{\gamma}$ is obtained using the Péclet number

$$Pe = \frac{\dot{\gamma} L_x^2}{D}, \quad (22)$$

where D is a representative diffusion coefficient value. Pe quantifies the advective transport strength by the flow relative to the diffusive transport strength. Given an experimental flow rate, details of determining $\dot{\gamma}$, which then yields Pe and \mathbf{v} for the computational setup, are provided in section S2 of the Supplementary Information document.

Flow rate values from 3.0 to 30.0 ml/min represent a reasonable range of experimental flow rates. For the computational cases in this study, a value of $Pe = 7.23 \times 10^6$ (corresponding to 3.0 ml/min) is used to represent a low flow rate, and a value of $Pe = 7.23 \times 10^7$ (corresponding to 30.0 ml/min) is used to represent a high flow rate.

2.4. Optimization methodology

2.4.1. Optimization parameterization and control variable definition

For a total number of sections N , each section's length is characterized using a set of N variables l_j , for $j = 0$ to $j = N - 1$. The optimization algorithm directly acts upon a set of $N - 1$ control variables ρ_j , for $j = 0$ to $j = N - 2$. Each length l_j is determined from the control variables ρ_j by the following procedure:

1. The first section length: $l_0 = \rho_0 \rho_1 \dots \rho_{N-2}$.
2. The intermediate section lengths (for $j = 1$ to $j = N - 2$): $l_j = \rho_0 \rho_1 \dots \rho_{N-(j+2)} (1 - \rho_{N-(j+1)})$.
3. The last section length: $l_{N-1} = 1 - \rho_0$.

Note that for $N = 2$, there are no intermediate sections, and so $l_0 = \rho_0$ and $l_1 = l_{N-1} = 1 - \rho_0$.

This procedure has been previously used in the design optimization literature^{37,38}, where it is referred to as the volume fraction relationships for N materials.

For regularization, section boundaries for each section are specified with a smoothed indicator function:

$$\chi_j(x) = 0.5 (\tanh(S(x - b_{\text{left},j})) - \tanh(S(x - b_{\text{right},j})), \quad (23)$$

where S is a sharpening parameter, and $b_{\text{left},j}$ and $b_{\text{right},j}$ are the left and right bounds, respectively, of each section j . As $S \rightarrow \infty$, $\chi_j(x)$ approaches an ideal indicator function (i.e., with sharp section definitions rather than smooth transition regions). While well-defined sections most accurately represent the intended catalyst surface boundary condition, using values of S that are too large results in undefined derivative values at the section boundaries, causing the optimization algorithm to fail to converge when computing the gradients needed for the adjoints. As a compromise, a sufficiently large value ($S > 10/l_j$) is used, allowing the sections to be distinctly defined while minimizing the extent and impact of intermediate values (χ_j values between 0 and 1).

2.4.2. Optimization procedure

The mathematical optimization problem is formulated as

$$\begin{aligned} \max_{\{\rho_j\}_{j=0}^{N-2}} \quad & \frac{1}{L_x} \int_0^{L_x} i_{\text{C}_2\text{H}_4, \text{local}} \, dx \\ \text{s.t.} \quad & \mathcal{F}(\mathbf{u}) = 0, \\ & 0 \leq \rho_j \leq L_x, \text{ for } j = 0, \dots, N-2, \end{aligned} \quad (24)$$

where $\mathcal{F}(\mathbf{u})$ represents the PDE system (forward problem) for the reactor, as presented in section 2.2, for a given catalyst patterning set by ρ_j . The specified constraints on ρ_j ensure that the total catalyst length L_x is preserved and that the sections do not overlap. A high-level depiction of how the optimization procedure interacts with the reactor simulation model is provided in fig. 1. The values of the system input parameters (flow rate, target applied voltage U_{max} , N) are specified, and the specific objective function is chosen as the goal of the optimization procedure. In this study, maximizing the spatial average of the local current density towards ethylene is chosen as the objective function.

If the target applied voltage value U_{max} is sufficiently negative, then the flow reactor solver does

not converge using the initial guess. In this case, a continuation loop is used to iteratively solve the system starting from a less negative U_{app} value and then gradually stepping towards U_{max} using an increment value ΔU . For this study, $\Delta U = 0.01$ V for $U_{app} \geq -1.55$ V vs. SHE, and $\Delta U = 0.005$ V for $U_{app} < -1.55$ V vs. SHE.

Each design iteration is performed as follows:

1. while $U_{app} > U_{max}$:
 - (a) solve governing system with strong regularization (smaller S in eq. (23)) and without the following species: H_2 , C_2H_4 , C_2H_6O , CH_4 (which do not affect the surface reaction performance and can thus be omitted to save cost)
 - (b) increment the applied voltage: $U_{app} += \Delta U$
2. solve adjoint problem of step 1
3. compute sensitivities
4. obtain optimized design pattern ($l_{j,opt}$)

This procedure is performed until convergence is satisfied, as described in section 2.5.

Using the final optimized design pattern, the final forward solve is performed as follows:

1. while $U_{app} > U_{max}$:
 - (a) solve governing system with optimized design pattern ($l_{j,opt}$), weaker regularization (larger S in eq. (23)), and with all species as specified in section 2.2.1
 - (b) increment the applied voltage: $U_{app} += \Delta U$
2. obtain final solution (solution fields and current densities)

2.5. Computational solver details

The flow and chemistry are solved using EchemFEM package^{39,40}, which is a Python package that utilizes the open-source finite element method (FEM) library Firedrake⁴¹. For spatial discretization, standard piecewise-linear elements are used with a Streamline Upwind Petrov-Galerkin (SUPG)^{42,43} stabilization scheme on the combined advection-migration flux⁴⁴. Additional details of the numerical implementation can be found in the references given.

For the optimization methodology (section 2.4), SciPy’s minimize function⁴⁵ is used as the minimization function, utilizing the limited-memory Broyden-Fletcher-Goldfarb-Shanno with bound constraints (L-BFGS-B) quasi-Newton method. Gradients are obtained with the adjoint method, which is done automatically via pyadjoint⁴⁶.

For the convergence criteria, the default options for the tolerances (function tolerance `ftol`, gradient tolerance `gtol`, and Jacobian numerical approximation step size `eps`) in SciPy’s L-BFGS-B method⁴⁵ are used.

3. Results and discussion

In this section, the results of the study are presented. To characterize the strengths of the surface reactions, two different applied voltage (U_{app}) values are considered. $U_{app} = -1.35$ V vs. the standard hydrogen electrode (SHE) represents a less negative (weaker surface reaction) case, and $U_{app} = -1.7$ V vs. SHE represents a more negative (stronger surface reaction) case. To characterize the electrolyte shear flow strength, two different values of the Péclet number Pe are considered, as mentioned and explained in section 2.3. $Pe = 7.23 \times 10^6$ (corresponding to a flow rate of 3.0 ml/min) is used as a low flow rate case, and $Pe = 7.23 \times 10^7$ (corresponding to a flow rate of 30.0 ml/min) is used as a high flow rate case.

3.1. Manually-patterned $N = 2$ cases

As an introduction and motivation prior to showing the optimization results, fig. 2 provides simulation results for cases that are set up and solved manually (using only the final forward solve procedure, skipping the optimization procedure in section 2.4.2). All of these electrode patterns use $N = 2$ and involve one Ag section upstream of one Cu section, as the simplest patterning configuration available for this work’s problem setup. As shown in fig. 2a, the Ag fraction d fully characterizes the patterning in this simplified configuration, creating an electrode consisting of one Ag section with length $= dL_x$ and one Cu section with length $= (1 - d)L_x$. The Ag fraction d is varied from $d = 0$ (for a fully Cu electrode) to $d = 1$ (for a fully Ag electrode), thus fully sweeping through the electrode patterning designs for $N = 2$.

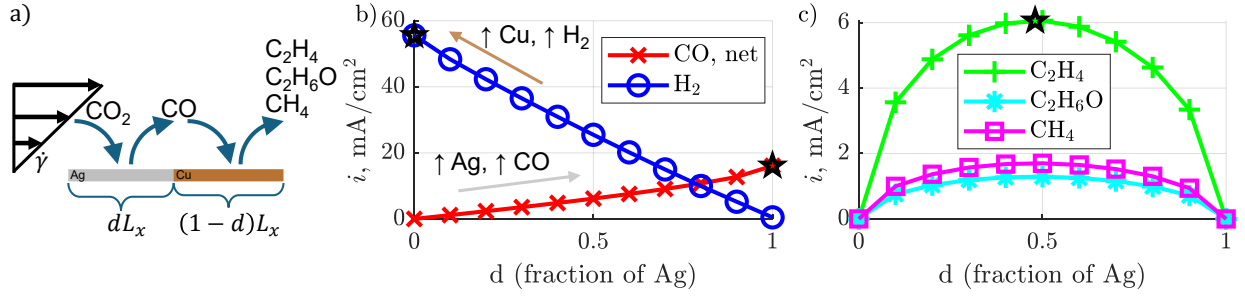


Figure 2: a) Schematic of the patterning configuration $N = 2$, along with the cascade reaction pathway considered: $\text{CO}_2 \longrightarrow \text{CO}$ for Ag, $\text{CO} \longrightarrow \{\text{C}_2\text{H}_4, \text{C}_2\text{H}_6\text{O}, \text{CH}_4\}$ for Cu. b) Plots of current density for net CO and for H₂, shown at 11 values of the Ag fraction ($d = 0$ through $d = 1$ in increments of 0.1). c) Plots of current density for C₂H₄, C₂H₆O, and CH₄, in the same format as for panel b. All cases shown use the same conditions as chosen in fig. 1: flow rate = 3.0 ml/min, $U_{app} = -1.7$ V vs. SHE. The maximum current density values and the corresponding value of d for CO (net), H₂, and C₂H₄ are shown for the appropriate curve with a black star; these maximum values have also been verified using the optimization procedure as presented in section 2.4.

In fig. 2b and fig. 2c, the current density i_k for each electrode product species k is plotted as a function of d . i_k is computed as a spatial average of the local current density $i_{k,local}$ (expression for each product species provided in section 2.2) over the length of the electrode,

$$i_k = \frac{1}{L_x} \int_0^{L_x} i_{k,local} dx. \quad (25)$$

Note that the H₂ current density i_{H_2} has contributions from both Ag and Cu. An important detail is that the CO current density shown is the net value, i.e. the quantity that would be measured in an experiment. CO is unique among the electrode products in this study's setup in that it is both produced (on Ag sections) and consumed (on Cu sections); thus, only integrating the CO current density from eq. (12) would only yield contribution from the production while neglecting the consumption. Thus, the plotted net CO current density $i_{\text{CO},net}$ is computed from the CO

production ($i_{\text{CO},+}$) and consumption ($i_{\text{CO},-}$) as

$$\begin{aligned} i_{\text{CO},\text{net}} &= i_{\text{CO},+} - i_{\text{CO},-}, \\ \text{with } i_{\text{CO},+} &= i_{\text{CO}}, \quad i_{\text{CO},-} = \frac{i_{\text{C}_2\text{H}_4}}{2} + \frac{i_{\text{C}_2\text{H}_6\text{O}}}{2} + \frac{i_{\text{CH}_4}}{3}, \end{aligned} \quad (26)$$

in order to account for the stoichiometric coefficients for the product species and electrons that participate in the reactions.

In fig. 2b, $i_{\text{CO},\text{net}}$ increases with Ag content ($d \rightarrow 1$), and i_{H_2} increases with Cu content ($d \rightarrow 0$). The optimal design is therefore trivially a pure Ag electrode for CO or a pure Cu electrode for H₂. Consequently, maximizing either CO or H₂ current density alone does not yield a meaningful optimization problem.

In contrast, as shown in fig. 2c, $i_{\text{C}_2\text{H}_4}$, $i_{\text{C}_2\text{H}_6\text{O}}$, and i_{CH_4} all show a maximum value at $d \simeq 0.5$, thus showing non-trivial optimal designs. To successfully maximize production of these products, the electrode patterning requires sufficient amounts of both Ag (to perform the $\text{CO}_2 \rightarrow \text{CO}$ conversion) and Cu (to perform the $\text{CO} \rightarrow \{\text{C}_2\text{H}_4, \text{C}_2\text{H}_6\text{O}, \text{CH}_4\}$ conversion). Insufficient section lengths of either electrode material (seen for d values near 0 and near 1) lead to inadequate contribution of one of these reaction sets in the tandem/cascade pathway, leading to overall suboptimal output. These three products – C₂H₄, C₂H₆O, and CH₄ – behave similarly to each other as a function of d , with only a simple scaling factor needed to approximate the current density profile of one given that of another. Thus, any of the three products can serve to illustrate the behavior of the Cu hydrocarbon products as a whole. For this reason and because the hydrocarbon products represent the value-added chemicals that are sought after in CO₂R, the maximum $i_{\text{C}_2\text{H}_4}$ is chosen as a representative objective function used in the optimization simulations presented through the rest of this study. Note that this similarity in profiles is likely a consequence of the chemistry modeling in this study. More realistic/accurate microkinetic modeling or experiments would likely show more complex relationships among the Cu product profiles. However, because other studies also generally show a positive correlation among these major Cu products², the general takeaways obtained by using the C₂H₄ current density as a representative metric should still hold.

The manual optimization sweep provides preliminary insight into reactor performance and optimiza-

tion objectives. While a systematic search is tractable for the single design variable case ($N = 2$), it becomes computationally unfeasible as N increases and the number of possible configurations grows exponentially. As demonstrated in section 3.2, higher hydrocarbon current densities can be achieved at larger N with optimized, often unintuitive, patterns. Nevertheless, the results here serve as a useful foundation for understanding reactor behavior prior to exploring more complex designs.

To quantify the product selectivity, fig. S4 of the Supplementary Information shows the Faradaic efficiency (FE) profile using the same flow rate and U_{app} conditions as used in fig. 2. Similar qualitative behavior is observed as in the current density behavior seen in fig. 2 and is discussed in section S7 of the Supplementary Information.

3.2. Effect of number of sections N , flow rate, and applied voltage U_{app} on optimized pattern

With the insight gained from the manual optimization results in section 3.1, our attention now turns to the results of cases generated using the design optimization methodology from section 2.4. A sweep of optimization cases results is shown in fig. 3. The initial configuration for all presented cases is equal section lengths ($l_j = L_x/N$ for each section j) with an alternating Ag/Cu/Ag/Cu/... pattern. Following the discussion in section 3.1, the objective function is chosen to be maximizing $i_{C_2H_4}$ for all optimization cases in this sweep.

The following parameter choices are used for the sweep:

1. Two applied voltage U_{app} conditions: The less negative value of $U_{app} = -1.35$ V vs. SHE results in a weaker surface reaction strength, and the more negative value of $U_{app} = -1.7$ V vs. SHE results in a stronger surface reaction strength.
2. Two flow rate values are chosen: 3.0 and 30.0 ml/min. These represent the lower and upper bounds of an example practical experimental flow rate, as discussed in section 2.3.
3. Three values of the number of sections N are chosen: $\{2, 6, 12\}$.

Figure 3a through fig. 3d show the patterns (section lengths and positions) for the optimized designs. For $N = 2$ designs, the optimized patterns for all conditions result in approximately 50% each for the Ag and Cu section lengths, regardless of the U_{app} and flow rate conditions. For $N = 2$, it is

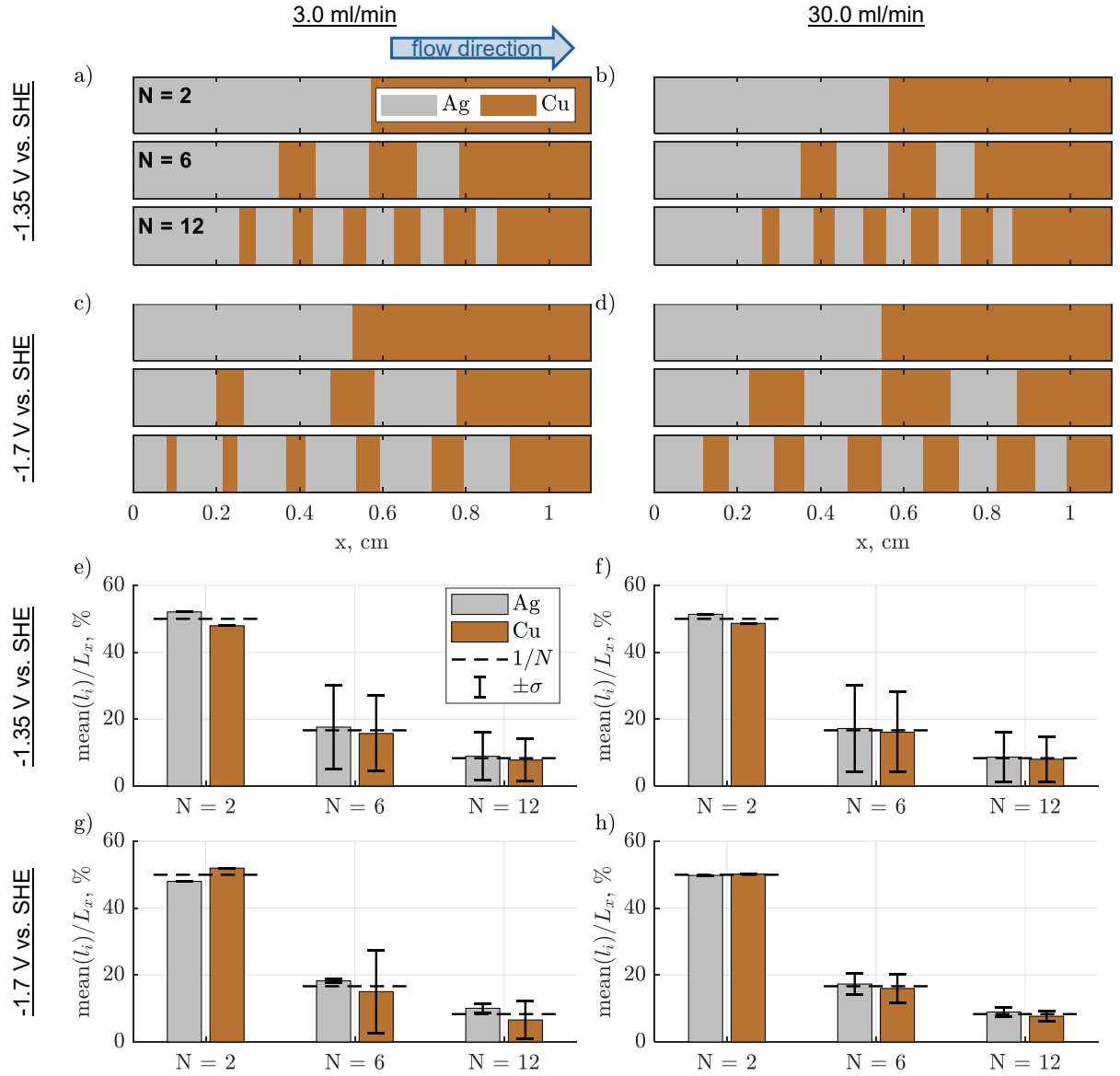


Figure 3: Plots of patterning and of section length statistics for optimized designs for various N , U_{app} , and flow rate values. a) - d) Optimized patterning showing section locations and length in x . e) - h) Mean Ag and Cu section lengths, normalized by electrode length L_x and shown as a percentage. Horizontal dashed lines for each N represent the section length for the equal length configuration ($l_j = L_x/N$ for each section j). Vertical error bars represent ± 1 standard deviation of the Ag and Cu section lengths.

evident that sufficient amounts of both catalysts are necessary to yield maximum C_2H_4 production; this is consistent with the findings from section 3.1. For the larger N values of 6 and 12, optimized patterns arise that display more interesting features and also show distinct patterns across the different combinations of U_{app} and flow rate conditions.

For the $U_{app} = -1.35$ V vs. SHE cases, the optimized patterns at larger N are characterized by long lengths for the first Ag section and the last Cu section. The intermediate Ag and Cu sections in the middle of the domain alternate rapidly, with each being significantly shorter than the first and last sections. These intermediate sections show slight gradients of shortening Ag and lengthening Cu section length moving along the flow direction. Interestingly, at this less negative U_{app} value, the optimized patterns are not appreciably different between the two different flow rate values.

For the $U_{app} = -1.7$ V vs. SHE cases, the optimized patterns at larger N display different features compared to the less negative U_{app} value and also show a significant dependency on flow rate. Starting with the high flow rate (30.0 ml/min) optimization case, the final optimized design displays only minimal deviation from the initial equal length configuration; the design also shows slight gradients of shortening Ag and lengthening Cu section lengths moving along the flow direction. It is observed in section 3.3 that these more negative U_{app} + high flow rate conditions correspond to the highest magnitude of C_2H_4 current density, implying that the initial equal length patterning is already high performing and close to the optimal design for these conditions. For the low flow rate (3.0 ml/min) optimization case, which is the most mass transport-limited case considered, the optimized patterning involves Ag sections that are all similar in length and Cu sections that noticeably increase in length along the flow direction.

Figure 3e through fig. 3h show the mean and standard deviations of the Ag and Cu section lengths for the optimized case design patterns across the flow rate/ U_{app} conditions. Note that the $N = 2$ optimized cases involve only one Ag section and one Cu section, and so their standard deviation is always equal to 0. Just as was observed in the section designs, a number of distinctive features appear in the section length mean and standard deviation values for the $U_{app} = -1.7$ V vs. SHE, flow rate = 3.0 ml/min conditions. Firstly, the total amount of Ag is favored over Cu, with the mean Ag section being $1.53\times$ longer than the mean Cu for $N = 12$. Secondly, at these conditions,

the standard deviation for Ag section lengths is significantly smaller than the Cu value; for all other conditions, the standard deviations of Ag and Cu section lengths are roughly equal. These attributes provide further evidence of the unique optimization behavior that occurs at the more negative U_{app} and low flow rate conditions.

3.3. Current density performance

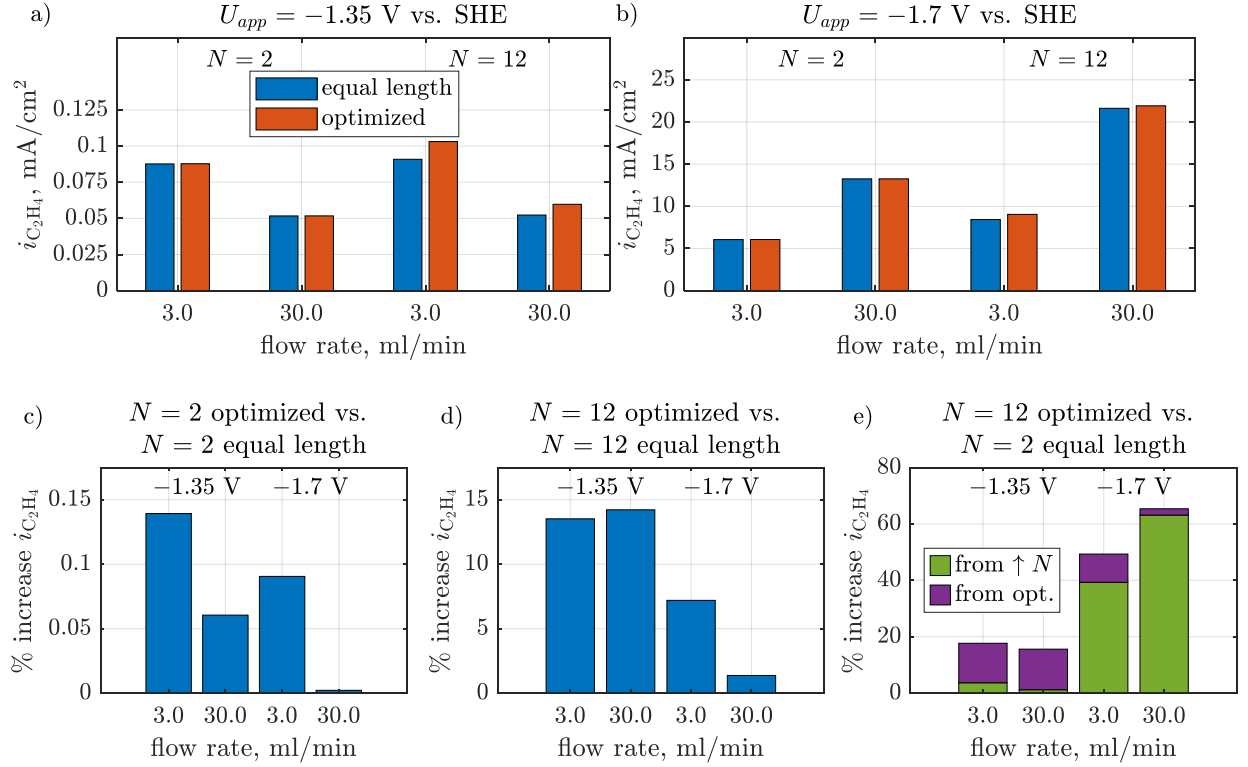


Figure 4: Plot of ethylene current density ($i_{C_2H_4}$) values and percentage increases relative to several baseline comparison values. All optimized cases shown here use $\max(i_{C_2H_4})$ as the objective function. a) $i_{C_2H_4}$, in mA/cm², for the less-negative applied voltage condition: $U_{app} = -1.35$ V vs. SHE. b) $i_{C_2H_4}$, in mA/cm², for the more-negative applied voltage condition: $U_{app} = -1.7$ V vs. SHE. c) Percentage increase in $i_{C_2H_4}$ for the optimized compared to the equal length cases, for $N = 2$. d) Percentage increase in $i_{C_2H_4}$ for the optimized compared to the equal length cases, for $N = 12$. e) Percentage increase in $i_{C_2H_4}$ for the $N = 12$ optimized compared to the $N = 2$ equal length cases. The percentage increase is separated into two contributions: from the increase in N , and from the optimization.

Figure 4 shows the values of the ethylene current density $i_{\text{C}_2\text{H}_4}$ for $N = 2$ and $N = 12$, across all combinations of applied voltage (U_{app}) and flow rate. From the values of $i_{\text{C}_2\text{H}_4}$ in fig. 4a and fig. 4b, some key trends emerge:

1. The values of $i_{\text{C}_2\text{H}_4}$ are significantly larger (by around two orders of magnitude) for the $U_{\text{app}} = -1.7$ V vs. SHE cases compared to the $U_{\text{app}} = -1.35$ V vs. SHE cases.
2. For a given U_{app} and flow rate, increasing N leads to increased $i_{\text{C}_2\text{H}_4}$, and the relative amount of increase is larger at more negative U_{app} .
3. Increased flow rates yield larger C_2H_4 current density values at the more negative $U_{\text{app}} = -1.7$ V vs. SHE, but yield smaller C_2H_4 current density values at the less negative $U_{\text{app}} = -1.35$ V vs. SHE.

Figure 4c and fig. 4d show the percentage increase in $i_{\text{C}_2\text{H}_4}$, for $N = 2$ in c and for $N = 12$ in d, when comparing the optimized patterning cases compared to the equal length patterning cases. Minimal % increase is achieved for $N = 2$ ($< 0.15\%$ across all U_{app} and flow rate values), while for $N = 12$ the % increase values are significantly larger (approaching 15% at $U_{\text{app}} = -1.35$ V vs. SHE).

The observed benefits in electrochemical performance for the best-performing cases can be divided into two contributing factors: 1) increasing the number of sections N and 2) optimizing their lengths. To emphasize and quantify these combined benefits of increased N and optimization, fig. 4e shows the % increase in $i_{\text{C}_2\text{H}_4}$ observed in the $N = 12$ optimized cases compared to the $N = 2$ equal length cases. All conditions yield significant percentage increases, with $\simeq 15 - 18\%$ at $U_{\text{app}} = -1.35$ V vs. SHE and $\simeq 50 - 65\%$ at $U_{\text{app}} = -1.7$ V vs. SHE. At $U_{\text{app}} = -1.35$ V vs. SHE, the optimization in patterning at the larger N is the predominant contribution towards the overall percentage increase. At $U_{\text{app}} = -1.7$ V vs. SHE, the opposite is true, with the increase N being by far the largest contribution.

As the key intermediate species in tandem CO_2R reaction systems, CO warrants further analysis of its current density behavior. For this purpose, fig. 5a and fig. 5b show the net CO current density $i_{\text{CO,net}}$, decomposed into the production $i_{\text{CO,+}}$ and consumption $i_{\text{CO,-}}$. Values are shown for the equal length case and the optimized case at all conditions for $N = 2$ and 12. The expressions for

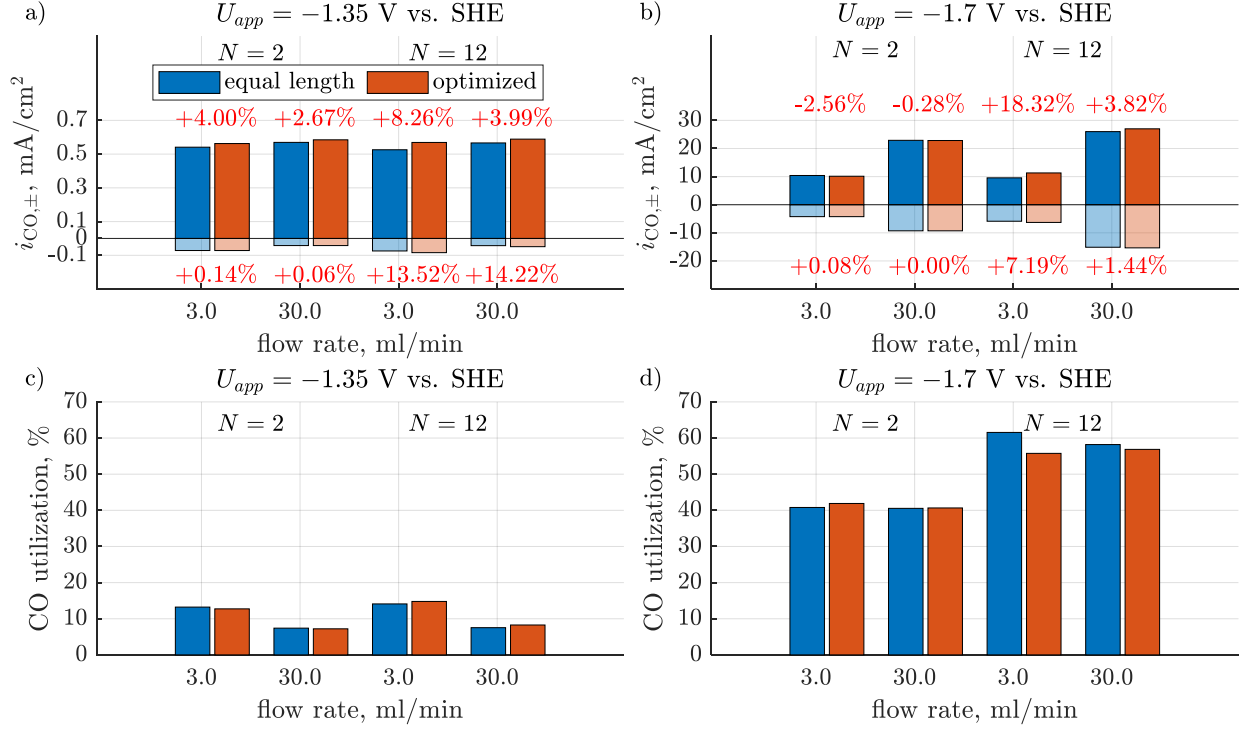


Figure 5: CO production $i_{CO,+}$ and consumption $i_{CO,-}$, as calculated from eq. (26), for the equal length case and optimized case of each condition, shown in a) for $U_{app} = -1.35$ V vs. SHE cases, and in b) for $U_{app} = -1.7$ V vs. SHE cases. For each case, the $i_{CO,-}$ value is multiplied by -1 and shown underneath the $i_{CO,+}$ bar, with the same color but lower opacity. Above each $i_{CO,+}$ pair of columns and below each $i_{CO,-}$ pair of columns, the percentage change of the optimized compared to the equal length value is shown. The CO utilization per eq. (27) is shown in c) for $U_{app} = -1.35$ V vs. SHE cases, and in d) for $U_{app} = -1.7$ V vs. SHE cases.

$i_{CO,+}$ and $i_{CO,-}$ are given in eq. (26).

It is observed that the magnitude of $i_{CO,-}$ in each optimized case is greater than or equal to the equal length case magnitude across all conditions and N values. Because CO is consumed in the production of C_2H_4 (see eq. (14)), increasing the CO consumption is necessary towards increasing $i_{C_2H_4}$ to satisfy the optimization objective function.

Towards increased understanding of this CO current density data, a parameter can be constructed that measures the proportion of the produced CO that is consumed by the Cu surface reactions,

i.e.

$$\text{CO utilization} = \frac{i_{\text{CO},-}}{i_{\text{CO},+}}. \quad (27)$$

Figure 5c and fig. 5d show the CO utilization values across the cases in this study. The less negative $U_{app} = -1.35$ V vs. SHE cases show utilization levels of less than 15% across all conditions, while the more negative $U_{app} = -1.7$ V vs. SHE cases show CO utilization values that are all substantially higher (all between 40% and 62%). However, for all conditions and N values as a whole, no significant increase (or decrease) in the CO utilization is observed for the optimized case values compared to the equal length case values.

When observing how the CO utilization depends on the flow rate, the behavior differs significantly at the two different U_{app} values considered, as discussed below.

For all of the less negative $U_{app} = -1.35$ V vs. SHE cases, increasing the flow rate causes a significant decrease in the CO utilization, with the 30.0 ml/min case values decreasing to 53.4 – 56.7% of the corresponding 3.0 ml/min case value. As seen in fig. 5a, the decreased CO utilization occurs because across all cases, for increased flow rate, $i_{\text{CO},+}$ increases slightly (by up to $\simeq 8\%$) while $i_{\text{CO},-}$ decreases significantly (by more than 57%). In short, despite a larger amount of produced CO that enters the system into the bulk electrolyte at the higher flow rate, the system is only about half as effective as it was at the lower flow rate in utilizing the CO using the Cu surface reactions. The underlying mechanism for this effect becomes clear in section 3.4 through observation of the combined interactions of the surface reaction strength and flow rate in the concentration fields.

Conversely, across all of the more negative $U_{app} = -1.7$ V vs. SHE cases, increasing the flow rate does not cause a significant decrease in CO utilization. Values in the 30.0 ml/min cases are within 94.5% of the corresponding 3.0 ml/min case value. Additionally, as seen in panel b of fig. 5, both the $i_{\text{CO},+}$ and $i_{\text{CO},-}$ more than double in value for 30.0 ml/min compared to the corresponding value at 3.0 ml/min. Thus, at the higher flow rate significantly more CO is generated, and even with this increased amount of CO the overall modeled reactor remains nearly as effective as at the lower flow rate in consuming the available CO via the Cu surface reactions. Just as was mentioned for the less negative U_{app} , this effect is explained by the impacts of surface reaction strength and flow rate in the concentration fields, as shown and discussed in section 3.4.

Tying these back to the reactor performance, increasing (or decreasing) the CO consumption directly contributes to an increase (or decrease) in $i_{\text{C}_2\text{H}_4}$, due to CO being the reactant species for the C_2H_4 electrochemical reaction. Thus, when considering the correlations of $i_{\text{C}_2\text{H}_4}$ with flow rate as seen in fig. 4, the inverse correlation at $U_{\text{app}} = -1.35$ V vs. SHE and the direct correlation at $U_{\text{app}} = -1.7$ V vs. SHE are both consistent with the CO consumption trends described here.

3.4. Analysis of concentration fields

The electrochemical performance results and discussion in section 3.3 focus on the electrode-averaged current density (i.e., the system-level performance). In this section, the concentration field results are presented, in order to gain insight into how the local environment features determine the overall flow reactor performance.

The first results presented in this section are the $N = 2$ equal length cases, in section 3.4.1. The goal is to isolate the key processes fundamental to the tandem reaction setup, which thus can be studied even in this simplest configuration of one Ag and one Cu section. Following this, the $N = 12$ results are presented in section 3.4.2, for both the optimized and the equal length patterning cases. With these more complicated cases, one introduced effect is that with increased patterning (with larger N), the Ag sections located further downstream from the leading edge can utilize any non-reacted CO_2 , thus producing more CO to be used by Cu sections also located downstream. Another introduced effect is that the optimized cases yield non-uniform Ag and Cu section lengths, causing more complicated species boundary layers growths and interactions. Understanding these effects that arise from increased patterning and optimized designs is important, as these cases yield noticeable increases in the overall current density performance (as seen in section 3.3).

3.4.1. Unoptimized equal length cases, $N = 2$

Figure 6 shows the contours and surface concentration profiles of CO_2 and CO for the $N = 2$ equal length cases. As seen in both the contours and the surface concentration profiles, the regions of low CO_2 and high CO concentrations clearly delineate the x -boundaries of the Ag section.

In the surface concentration profiles, the sharpness of the concentration gradients (dc_k/dx) at the section boundaries provides a sense of the relative surface reaction strength, with the $U_{\text{app}} = -1.7$

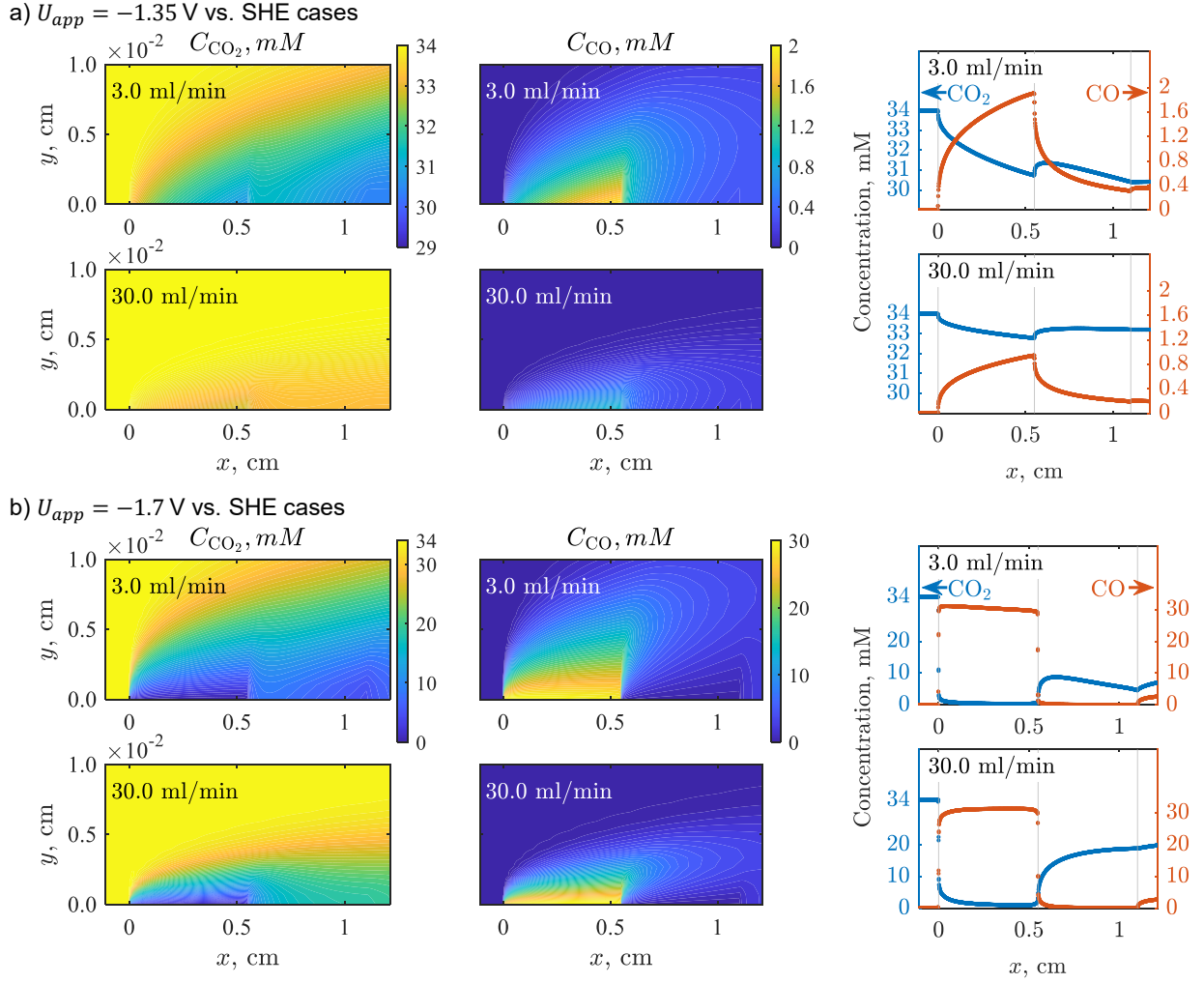


Figure 6: Concentration field contour plots and surface concentration line plots for CO_2 and CO , for the equal length patterning with $N = 2$. Plots are shown for a) the less negative $U_{app} = -1.35$ V vs. SHE applied voltage, and for b) the more negative $U_{app} = -1.7$ V vs. SHE applied voltage. For the surface concentrations plots, vertical gray lines denote the locations of the section boundaries.

V vs. SHE gradients all being much sharper (corresponding to the stronger reaction rates for both Ag and Cu). It is also observed that large proportions of Cu sections near the downstream trailing edge exhibit low CO surface concentrations; these “dead zones” yield only minimal production of Cu products. It is shown and discussed in section 3.4.2 that reducing the existence and impact of these dead zones is a key hypothesis of how the optimized designs maximize the CO consumption to maximize the ethylene current density objective.

The $U_{app} = -1.35$ V vs. SHE contours and profiles exhibit a strong dependency on flow rate, with the higher flow rate showing significantly larger CO_2 concentrations and smaller CO concentrations. On the other hand, the $U_{app} = -1.7$ V vs. SHE plots show only minor differences between the low and high flow rate plots. These differences arise from how CO_2 and CO each enter the system, combined with the relative strengths of the flow rate compared to the surface reactions; these behaviors are discussed here below.

CO_2 : Because CO_2 is fed into the system at the inlet at 34 mM for each case, its supply is always guaranteed to reach the surface of the first Ag section. Regardless of U_{app} , increasing the flow rate more effectively replenishes high concentration CO_2 fluid onto the Ag section surface, which increases the CO production (as reflected in fig. 5).

CO: On the other hand, CO is not supplied into the system at the inlet, as it must be created through the Ag surface reaction. This “non-guaranteed” supply means that its behavior in response to flow rate depends on the relative surface reaction strength.

At $U_{app} = -1.35$ V vs. SHE, the weaker surface reaction strength is overcome by the flow strength; thus, the flow sweeps the CO downstream such that high concentrations are unable to accumulate above the Ag section surface. Thus, the already limited supply of CO that reaches Cu surface is made even more scarce at high flow rates. This behavior mechanistically explains why the increased flow rate causes a decrease in CO consumption as seen in fig. 5 and thus leads to the decrease in $i_{\text{C}_2\text{H}_4}$ as seen in fig. 4.

At $U_{app} = -1.7$ V vs. SHE, the stronger surface reaction strength overcomes the flow strength, so that high CO concentrations are able to accumulate on the Ag for both slow and fast flow rates. The high CO concentrations that are generated on the Ag surface “guarantees” its supply to reach the Cu section, much like the CO_2 for Ag. Increasing the flow rate thus increases the replenishment of high CO to reach the Cu surface, contributing to the increased CO consumption as seen in fig. 5 and thus leading to the increased $i_{\text{C}_2\text{H}_4}$ as seen in fig. 4.

As a note, as seen in fig. 6, the surface concentration of CO can exceed the 0.95 mM solubility limit. This gas supersaturation near the electrode surface is a well-documented effect, especially for smooth electrode surfaces that are capable of suppressing bubble nucleation¹².

3.4.2. Equal length and optimized cases, $N = 12$

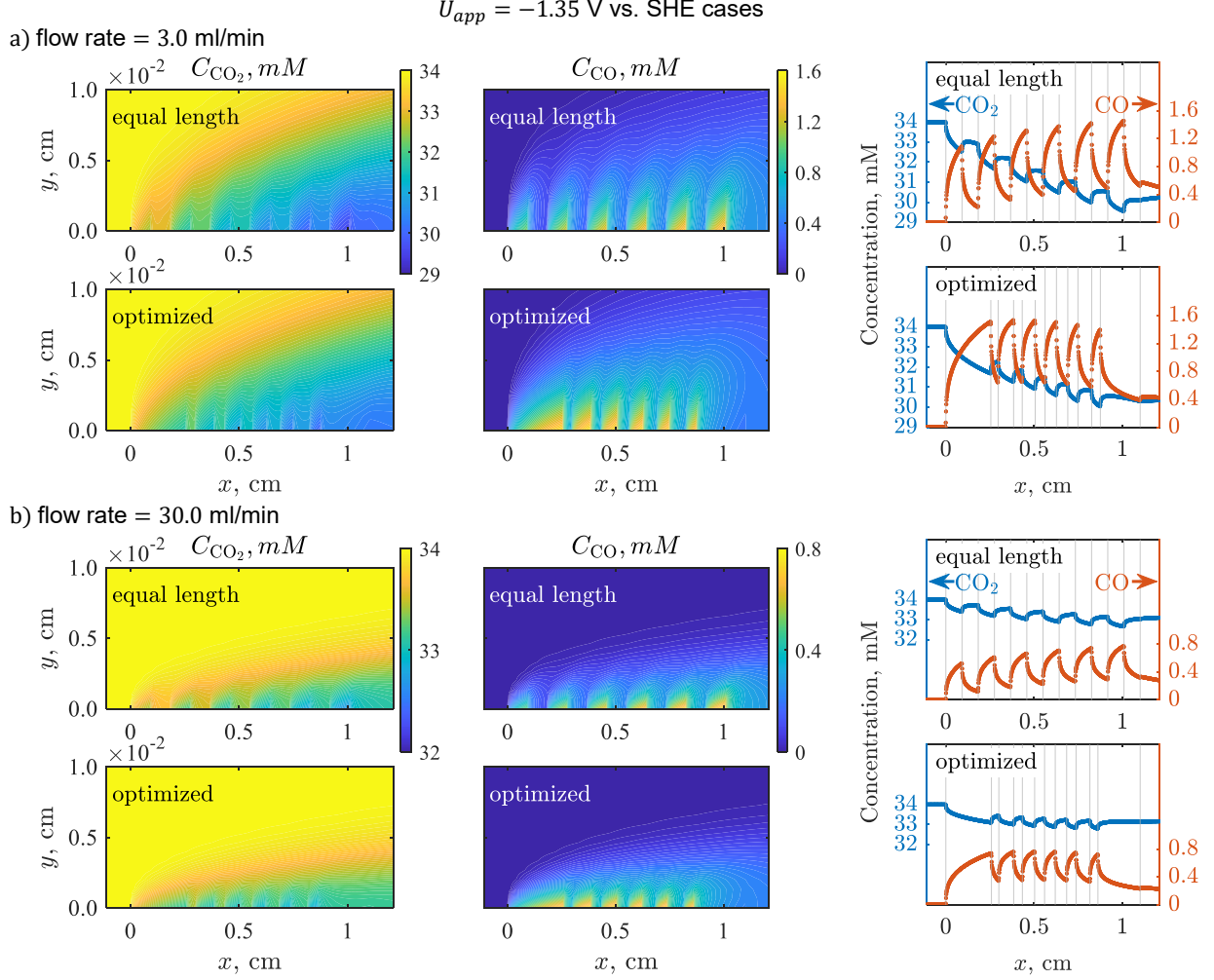


Figure 7: Concentration field contour plots and surface concentration line plots for CO_2 and CO , for both the equal length and optimized patternings for the less negative $U_{app} = -1.35$ V vs. SHE applied voltage. Plots are shown for a) the lower 3.0 ml/min flow rate cases, and for b) the higher 30.0 ml/min flow rate cases. For the surface concentrations plots, vertical gray lines denote the locations of the section boundaries.

Armed with intuition from the $N = 2$ cases, we are now prepared to analyze the more complex $N = 12$ cases. Figure 7 shows the concentration field contours and surface concentration profiles for the $N = 12$ cases at $U_{app} = -1.35$ V vs. SHE. As is also observed in the $N = 2$ equal length cases, the CO_2 concentration stays high along the electrode surface (due to the limited consumption by the

weak Ag surface reaction), especially at the higher flow rate. An effect that is only seen with larger N values, in the equal length cases at each flow rate, is that the CO surface concentration steadily increases moving downstream, as the CO that was not consumed from the preceding upstream Cu section combines with the CO production of each subsequent Ag section to accumulate on that Ag section.

Now shifting focus towards the optimized designs, the design patternings (as also shown in fig. 3) feature long lengths for the first Ag and the last Cu sections, with alternating short sections in between. For the optimized case for each flow rate in fig. 7, the first long Ag section yields a noticeably higher peak surface CO concentration than in the corresponding equal length case. The shorter intermediate Ag and Cu sections then work together to preserve the surface CO concentration at a higher minimum value and higher average value overall than in the corresponding equal length case. Compared to the corresponding equal length case, the increased CO concentration for the optimized cases reflects the higher overall CO production, which also yields increased reactant supply for the Cu surface reactions and ultimately leads to increased CO consumption towards satisfying the objective of maximizing C_2H_4 current density. The CO production and consumption for these $N = 12, U_{app} = -1.35$ V vs. SHE cases are consistent with the data shown in fig. 5. Finally, the final long Cu section consumes as much of the remaining CO as possible as the fluid moves towards the domain exit.

Now moving to the more negative applied voltage, fig. 8 shows the concentration field contours and surface concentration profiles for the $N = 12$ cases at $U_{app} = -1.7$ V vs. SHE. In these cases, as is also observed in the $N = 2$ equal length cases, the strong strength of the surface reactions causes the Ag sections to consume significant CO_2 (concentration $\rightarrow 0$) and produce significant CO, and also causes the Cu sections to consume significant CO (concentration $\rightarrow 0$). As expected, at the faster flow rate, the reactant concentrations are higher due to the increased mass transport, which causes high reactant concentration fluid to be transported to the downstream catalyst sections' surfaces.

For the equal length cases at both flow rates, the surface concentration of CO on the Cu sections consistently reaches a lower value than that of CO_2 on the Ag sections. While visible from the

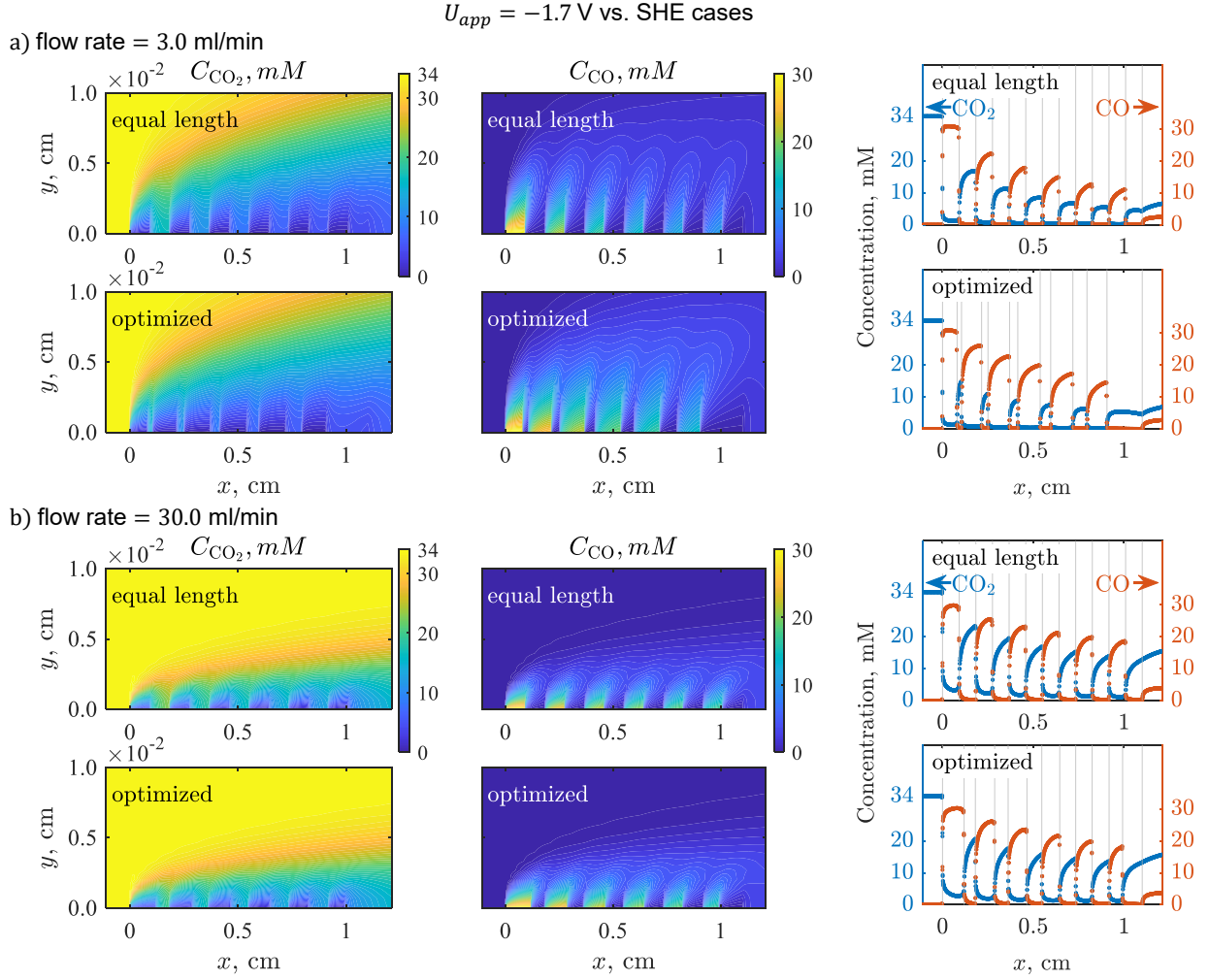


Figure 8: Concentration field contour plots and surface concentration line plots for CO_2 and CO , for both the equal length and optimized patternings for the more negative $U_{app} = -1.7 \text{ V vs. SHE}$ applied voltage. Plots are shown for a) the lower 3.0 ml/min flow rate cases, and for b) the higher 30.0 ml/min flow rate cases. For the surface concentrations plots, vertical gray lines denote the locations of the section boundaries.

surface concentration plots, this comparison is made clearer using plots of the averaged surface concentrations in section S8 of the Supplementary Information. Thus, it is hypothesized that in the equal length patterns, the “dead zones” of low CO reactant on Cu sections are more prevalent and have a larger impact in reducing the system performance compared to the “dead zones” of low CO_2 reactant on Ag sections.

We now turn our focus to the patterning design and the resulting concentration behavior of the optimized cases. As is pointed out in section 3.2, the optimized patterns for these $U_{app} = -1.7$ V vs. SHE cases feature longer Ag sections at the expense of shortened Cu sections, especially for the low flow rate case. By shortening the Cu sections, the optimized designs minimize the more detrimental negative impact of the CO “dead zones”, opting to allocate the unused length to create longer Ag sections to yield increased CO production. This leads to increased reactant CO concentration on the Cu sections, which thus leads to increased CO consumption. In summary, our interpretation of the optimization algorithm’s behavior at the stronger surface reaction conditions is that the lost consumption from removing the “dead zone” Cu regions is outweighed by increasing the Ag section lengths to produce more CO. Overall, this leads to increased CO consumption and increased $i_{C_2H_4}$, thus satisfying the objective function.

4. Conclusions

Towards exploring design principles for higher performance CO₂R electrolyzers, this work presents a computational simulation framework that combines continuum transport modeling, tandem catalysis, and design optimization in a flow reactor case study. In the tandem catalyst patterning, Ag sections provides the $CO_2 \longrightarrow CO$ reaction capability, and Cu sections provides the $CO \longrightarrow$ high-value products reaction capability.

A parameter sweep is performed for the surface applied voltage U_{app} , the electrolyte flow rate, and the number of sections N . Cases are run for equal length patterns and for optimized patterns (which maximize the current density towards ethylene, $i_{C_2H_4}$, as the objective function). For the resultant optimized section patterns, less negative U_{app} (weaker surface reaction) conditions favor longer first and last sections with shorter intermediate sections. Optimized patterns for more negative U_{app} (stronger surface reaction) conditions are largely more uniform in section length but show a flow rate dependency.

The reactor performance, assessed using $i_{C_2H_4}$, demonstrates a % increase for the optimized cases that can be decomposed into two contributing components: 1) from increased N , and 2) from optimization. The contribution from optimization dominates the % increase at less negative U_{app} ,

while the contribution from increased N dominates at more negative U_{app} . The highest performance increases in this study occur at the more negative $U_{app} = -1.7$ V vs. SHE value: using $N = 12$ sections, % increases in $i_{C_2H_4}$ of up to 65% are achieved compared to the corresponding unoptimized equal-length $N = 2$ cases. Analysis of the concentration fields provides mechanistic insight to explain the final optimized patterns. The key goal of the optimized patterns is to minimize regions of low CO concentration on the Cu section surfaces, thus maximizing C_2H_4 production. Because CO is the reaction system’s key intermediate species, trends in CO production and consumption closely align with the concentration field observations.

This work demonstrates that the combination of informed continuum modeling with high performance computing (HPC) tools to drive design optimization provides a powerful method for studying electrochemical processes. Future directions of work include investigating other reaction systems, investigating other design optimization objective functions (such as selectivity or energy efficiency metrics), or modifying the setup to allow for optimization of operating conditions including U_{app} and flow rate. Another potential future direction is to extend the developed optimization capability to three-dimensional (3D) settings, such as gas diffusion electrodes (GDEs), modifications of the flow field, and other complex cell configurations. Forward analysis of 3D setups in previous studies, such as modified Ag/Cu catalyst layer segment lengths and loadings in GDEs⁵, have yielded complementary findings to the insights from the current study; thus, applying design optimization to such configurations is a logical next step for future studies. For 3D settings, incorporating shape/topology optimization capabilities for electrode morphology modification also comes into play. In experimental settings, the capabilities presented in this work help narrow the space of possible designs to focus on parameter choices and setups with high performance promise.

5. Acknowledgments

This work was performed under the auspices of the U.S. Department of Energy by Lawrence Livermore National Laboratory (LLNL) under Contract No. DE-AC52-07NA27344, and was partially supported by a Cooperative Research and Development Agreement (CRADA) between LLNL and TotalEnergies American Services, Inc. (affiliate of TotalEnergies SE) under Agreement No.

TC02307. This work was supported by the Korea Institute of Energy Technology Evaluation and Planning (KETEP) and the Ministry of Trade, Industry & Energy (MOTIE) of the Republic of Korea (RS-2024-00488176) through funding to J.-W.J. LLNL release number: LLNL-JRNL-2012882.

ORCID iDs

1. Jack Guo: 0000-0003-4090-9289
2. Thomas Roy: 0000-0002-4286-4507
3. Nitish Govindarajan: 0000-0003-3227-5183
4. Joel B. Varley: 0000-0002-5384-5248
5. Jonathan Raison: 0009-0009-6455-599X
6. Jinyoung Lee: 0000-0002-6905-896X
7. Jiwook Jang: 0000-0003-1251-1011
8. Dong Un Lee: 0000-0001-7591-5350
9. Thomas F. Jaramillo: 0000-0001-9900-0622
10. Tiras Y. Lin: 0000-0002-3377-9933

References

- [1] Stephens, I. E.; Chan, K.; Bagger, A.; Boettcher, S. W.; Bonin, J.; Boutin, E.; Buckley, A. K.; Buonsanti, R.; Cave, E. R.; Chang, X.; others 2022 roadmap on low temperature electrochemical CO₂ reduction. *Journal of Physics: Energy* **2022**, *4*, 042003.
- [2] Nitopi, S.; Bertheussen, E.; Scott, S. B.; Liu, X.; Engstfeld, A. K.; Horch, S.; Seger, B.; Stephens, I. E.; Chan, K.; Hahn, C.; others Progress and perspectives of electrochemical CO₂ reduction on copper in aqueous electrolyte. *Chemical reviews* **2019**, *119*, 7610–7672.
- [3] Burdyny, T.; Smith, W. A. CO₂ reduction on gas-diffusion electrodes and why catalytic performance must be assessed at commercially-relevant conditions. *Energy & Environmental Science* **2019**, *12*, 1442–1453.

- [4] Duarte, M.; De Mot, B.; Hereijgers, J.; Breugelmans, T. Electrochemical reduction of CO₂: effect of convective CO₂ supply in gas diffusion electrodes. *ChemElectroChem* **2019**, *6*, 5596–5602.
- [5] Zhang, T.; Bui, J. C.; Li, Z.; Bell, A. T.; Weber, A. Z.; Wu, J. Highly selective and productive reduction of carbon dioxide to multicarbon products via in situ CO management using segmented tandem electrodes. *Nature Catalysis* **2022**, *5*, 202–211.
- [6] Bui, J. C.; Lees, E. W.; Pant, L. M.; Zenyuk, I. V.; Bell, A. T.; Weber, A. Z. Continuum modeling of porous electrodes for electrochemical synthesis. *Chemical reviews* **2022**, *122*, 11022–11084.
- [7] Moore, T.; Xia, X.; Baker, S. E.; Duoss, E. B.; Beck, V. A. Elucidating mass transport regimes in gas diffusion electrodes for CO₂ electroreduction. *ACS Energy Letters* **2021**, *6*, 3600–3606.
- [8] Weng, L.-C.; Bell, A. T.; Weber, A. Z. Modeling gas-diffusion electrodes for CO₂ reduction. *Physical Chemistry Chemical Physics* **2018**, *20*, 16973–16984.
- [9] Bohra, D.; Chaudhry, J. H.; Burdyny, T.; Pidko, E. A.; Smith, W. A. Modeling the electrical double layer to understand the reaction environment in a CO₂ electrocatalytic system. *Energy & Environmental Science* **2019**, *12*, 3380–3389.
- [10] Wei, C.; Yang, Y.; Ma, H.; Sun, G.; Wang, X.; Cheng, Y.; Zhang, C.; Yeo, B. S.; He, C.; Wong, A. B. Nanoscale Management of CO Transport in CO₂ Electroreduction: Boosting Faradaic Efficiency to Multicarbon Products via Nanostructured Tandem Electrocatalysts. *Advanced Functional Materials* **2023**, 2214992.
- [11] Gurudayal; Perone, D.; Malani, S.; Lum, Y.; Haussener, S.; Ager, J. W. Sequential cascade electrocatalytic conversion of carbon dioxide to C–C coupled products. *ACS Applied Energy Materials* **2019**, *2*, 4551–4559.
- [12] Lum, Y.; Ager, J. W. Sequential catalysis controls selectivity in electrochemical CO₂ reduction on Cu. *Energy & Environmental Science* **2018**, *11*, 2935–2944.

- [13] Zhang, B.; Wang, L.; Li, D.; Li, Z.; Bu, R.; Lu, Y. Tandem strategy for electrochemical CO₂ reduction reaction. *Chem Catalysis* **2022**, *2*, 3395–3429.
- [14] Zhu, Y.; Cui, X.; Liu, H.; Guo, Z.; Dang, Y.; Fan, Z.; Zhang, Z.; Hu, W. Tandem catalysis in electrochemical CO₂ reduction reaction. *Nano Research* **2021**, 1–16.
- [15] Lin, Y.-R.; Lee, D. U.; Tan, S.; Koshy, D. M.; Lin, T. Y.; Wang, L.; Corral, D.; Avilés Acosta, J. E.; Zamora Zeledon, J. A.; Beck, V. A.; Baker, S. E.; Duoss, E. B.; Hahn, C.; Jaramillo, T. F. Vapor-Fed Electrolyzers for Carbon Dioxide Reduction Using Tandem Electrocatalysts: Cuprous Oxide Coupled with Nickel-Coordinated Nitrogen-Doped Carbon. *Advanced Functional Materials* **2022**, *32*, 2113252.
- [16] Hori, Y.; Kikuchi, K.; Suzuki, S. Production of CO and CH₄ in electrochemical reduction of CO₂ at metal electrodes in aqueous hydrogencarbonate solution. *Chemistry letters* **1985**, *14*, 1695–1698.
- [17] Hori, Y.; Kikuchi, K.; Murata, A.; Suzuki, S. Production of methane and ethylene in electrochemical reduction of carbon dioxide at copper electrode in aqueous hydrogencarbonate solution. *Chemistry Letters* **1986**, *15*, 897–898.
- [18] Hori, Y.; Murata, A.; Takahashi, R.; Suzuki, S. Enhanced formation of ethylene and alcohols at ambient temperature and pressure in electrochemical reduction of carbon dioxide at a copper electrode. *Journal of the Chemical Society, Chemical Communications* **1988**, 17–19.
- [19] Hori, Y.; Murata, A.; Takahashi, R. Formation of hydrocarbons in the electrochemical reduction of carbon dioxide at a copper electrode in aqueous solution. *Journal of the Chemical Society, Faraday Transactions 1: Physical Chemistry in Condensed Phases* **1989**, *85*, 2309–2326.
- [20] Hori, Y.; Wakebe, H.; Tsukamoto, T.; Koga, O. Electrocatalytic process of CO selectivity in electrochemical reduction of CO₂ at metal electrodes in aqueous media. *Electrochimica Acta* **1994**, *39*, 1833–1839.

- [21] Chen, C.; Li, Y.; Yu, S.; Louisia, S.; Jin, J.; Li, M.; Ross, M. B.; Yang, P. Cu-Ag tandem catalysts for high-rate CO₂ electrolysis toward multicarbons. *Joule* **2020**, *4*, 1688–1699.
- [22] Wang, Y.; Wang, D.; Dares, C. J.; Marquard, S. L.; Sheridan, M. V.; Meyer, T. J. CO₂ reduction to acetate in mixtures of ultrasmall (Cu)_n(Ag)_m bimetallic nanoparticles. *Proceedings of the National Academy of Sciences* **2018**, *115*, 278–283.
- [23] Morales-Guio, C. G.; Cave, E. R.; Nitopi, S. A.; Feaster, J. T.; Wang, L.; Kuhl, K. P.; Jackson, A.; Johnson, N. C.; Abram, D. N.; Hatsukade, T.; others Improved CO₂ reduction activity towards C₂₊ alcohols on a tandem gold on copper electrocatalyst. *Nature Catalysis* **2018**, *1*, 764–771.
- [24] Martins, J. R.; Ning, A. *Engineering design optimization*; Cambridge University Press, 2021.
- [25] Tortorelli, D. Solid mechanics: analysis and design with the Finite Element Method. *Electronic Publication, Urbana* **2010**,
- [26] Giles, M. B.; Pierce, N. A. An introduction to the adjoint approach to design. *Flow, turbulence and combustion* **2000**, *65*, 393–415.
- [27] Nachbagauer, K.; Oberpeilsteiner, S.; Sherif, K.; Steiner, W. The use of the adjoint method for solving typical optimization problems in multibody dynamics. *Journal of Computational and Nonlinear Dynamics* **2015**, *10*, 061011.
- [28] Roy, T.; Salazar de Troya, M. A.; Worsley, M. A.; Beck, V. A. Topology optimization for the design of porous electrodes. *Structural and Multidisciplinary Optimization* **2022**, *65*, 171.
- [29] Yaji, K.; Yamasaki, S.; Tsushima, S.; Suzuki, T.; Fujita, K. Topology optimization for the design of flow fields in a redox flow battery. *Structural and multidisciplinary optimization* **2018**, *57*, 535–546.
- [30] Alizadeh, M.; Charoen-Amornkitt, P.; Suzuki, T.; Tsushima, S. Recent advances in electrode optimization of electrochemical energy devices using topology optimization. *Progress in Energy* **2024**, *7*, 012003.

- [31] Lin, T. Y.; Baker, S. E.; Duoss, E. B.; Beck, V. A. Topology optimization of 3D flow fields for flow batteries. *Journal of The Electrochemical Society* **2022**, *169*, 050540.
- [32] Schulz, K. G.; Riebesell, U.; Rost, B.; Thoms, S.; Zeebe, R. Determination of the rate constants for the carbon dioxide to bicarbonate inter-conversion in pH-buffered seawater systems. *Marine chemistry* **2006**, *100*, 53–65.
- [33] Corpus, K. R. M.; Bui, J. C.; Limaye, A. M.; Pant, L. M.; Manthiram, K.; Weber, A. Z.; Bell, A. T. Coupling covariance matrix adaptation with continuum modeling for determination of kinetic parameters associated with electrochemical CO₂ reduction. *Joule* **2023**,
- [34] Li, J.; Chang, X.; Zhang, H.; Malkani, A. S.; Cheng, M.-J.; Xu, B.; Lu, Q. Electrokinetic and in situ spectroscopic investigations of CO electrochemical reduction on copper. *Nature communications* **2021**, *12*, 3264.
- [35] Kuhl, K. P.; Cave, E. R.; Abram, D. N.; Jaramillo, T. F. New insights into the electrochemical reduction of carbon dioxide on metallic copper surfaces. *Energy & Environmental Science* **2012**, *5*, 7050–7059.
- [36] Corral, D.; Lee, D. U.; Ehlinger, V. M.; Nitopi, S.; Acosta, J. E. A.; Wang, L.; King, A. J.; Feaster, J. T.; Yi-Rung, L.; Weber, A. Z.; Baker, S. E.; Duoss, E. B.; Beck, V. A.; Hahn, C.; Jaramillo, T. F. Bridging knowledge gaps in liquid-and vapor-fed CO₂ electrolysis through active electrode area. *Chem Catalysis* **2022**, *2*, 3239–3253.
- [37] Sigmund, O.; Torquato, S. Design of materials with extreme thermal expansion using a three-phase topology optimization method. *Journal of the Mechanics and Physics of Solids* **1997**, *45*, 1037–1067.
- [38] Watts, S.; Tortorelli, D. A. An n -material thresholding method for improving integerness of solutions in topology optimization. *International Journal for Numerical Methods in Engineering* **2016**, *108*, 1498–1524.
- [39] Roy, T.; Andrej, J.; Antimes, A.; Beck, V. A.; Ehlinger, V.; Euzenat, F.; Govindarajan, N.;

- Guo, J.; Lin, T. Y.; Moore, T. EchemFEM: A Firedrake-based Python package for electrochemical transport. *Journal of Open Source Software* **2024**, *9*, 6531.
- [40] Roy, T.; Andrej, J.; Beck, V. A. A scalable DG solver for the electroneutral Nernst-Planck equations. *Journal of Computational Physics* **2023**, *475*, 111859.
- [41] Ham, D. A. et al. Firedrake user manual. Imperial College London; University of Oxford; Baylor University; University of Washington., 2023; Available at <https://doi.org/10.25561/104839>.
- [42] Brooks, A. N.; Hughes, T. J. Streamline upwind/Petrov-Galerkin formulations for convection dominated flows with particular emphasis on the incompressible Navier-Stokes equations. *Computer methods in applied mechanics and engineering* **1982**, *32*, 199–259.
- [43] Elman, H. C.; Silvester, D.; Wathen, A. *Finite elements and fast iterative solvers, Numerical Mathematics and Scientific Computation*, 2nd ed.; Oxford University Press, 2014.
- [44] Govindarajan, N.; Lin, T. Y.; Roy, T.; Hahn, C.; Varley, J. B. Coupling Microkinetics with Continuum Transport Models to Understand Electrochemical CO₂ Reduction in Flow Reactors. *PRX Energy* **2023**, *2*, 033010.
- [45] Virtanen, P. et al. SciPy 1.0: Fundamental Algorithms for Scientific Computing in Python. *Nature Methods* **2020**, *17*, 261–272.
- [46] Mitusch, S. K.; Funke, S. W.; Dokken, J. S. dolfin-adjoint 2018.1: automated adjoints for FEniCS and Firedrake. *Journal of Open Source Software* **2019**, *4*, 1292.

TOC Graphic

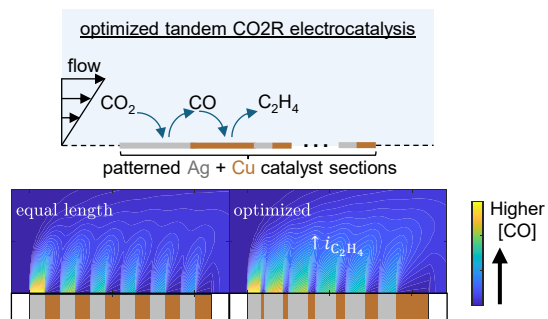


Figure 9: TOC Graphic.

Supplementary information

Optimized tandem catalyst patterning for CO₂ reduction flow reactors

Jack Guo^{a,*}, Thomas Roy^a, Nitish Govindarajan^b, Joel B. Varley^b, Jonathan Raison^{c,e}, Jinyoung Lee^{c,d,f}, Jiwook Jang^{f,g}, Dong Un Lee^{c,d}, Thomas F. Jaramillo^{c,d}, Tiras Y. Lin^{a,*}

^a*Computational Engineering Division, Lawrence Livermore National Laboratory, Livermore, CA 94550, USA*

^b*Materials Science Division, Lawrence Livermore National Laboratory, Livermore, CA 94550, USA*

^c*SUNCAT Center for Interface Science and Catalysis, Department of Chemical Engineering, Stanford University, Stanford, CA 94305, USA*

^d*SUNCAT Center for Interface Science and Catalysis, SLAC National Accelerator Laboratory, Menlo Park, CA 94025, USA*

^e*TotalEnergies Research & Technology USA LLC, Houston, TX 77002, USA*

^f*School of Energy and Chemical Engineering, Ulsan National Institute of Science and Technology (UNIST), Ulsan, Republic of Korea*

^g*Graduate School of Carbon Neutrality, Ulsan National Institute of Science and Technology (UNIST), Ulsan, Republic of Korea*

Contents

S1 Tabulated values	2
S2 Fluid flow modeling details	4
S3 Ag surface chemistry formulation	5
S4 Ag surface chemistry validation of implementation	7
S5 Cu surface chemistry formulation	9
S6 Cu surface chemistry validation	10
S7 Manually-patterned $N = 2$ cases, Faradaic Efficiency (FE)	12
S8 Average surface concentrations of CO₂, CO, C₂H₄	13

*Corresponding author

Email addresses: guo9@llnl.gov (Jack Guo), lin46@llnl.gov (Tiras Y. Lin)

S1. Tabulated values

Table S1: Table of diffusivity values for each chemical species.

Diffusivity	Value ($\text{m}^2 \text{s}^{-1}$)	Ref.
D_{CO_2}	1.91×10^{-9}	[1]
D_{K^+}	1.957×10^{-9}	[1]
D_{OH^-}	5.29×10^{-9}	[1]
D_{H^+}	9.311×10^{-9}	[1]
$D_{\text{CO}_3^{2-}}$	0.92×10^{-9}	[1]
$D_{\text{HCO}_3^-}$	1.185×10^{-9}	[1]
D_{CO}	2.03×10^{-9}	[2]
D_{H_2}	4.50×10^{-9}	[2]
$D_{\text{C}_2\text{H}_4}$	1.87×10^{-9}	[2]
$D_{\text{C}_2\text{H}_6\text{O}}$	0.84×10^{-9}	[2]
D_{CH_4}	1.49×10^{-9}	[2]

Table S2: Table of reaction rate constant values for the reactions in the bulk bicarbonate electrolyte (as listed in eq. (1) in the main text). For bulk reaction index j , certain values are provided in terms of the equilibrium constant K_j and the dissociation constant of water K_w .

Rxn. rate	Value & Units	Ref.	Rxn. rate	Value & Units	Ref.
K_1	$10^{-6.37} \text{ mol L}^{-1}$	[1]	k_{2f}	$3.71 \times 10^{-2} \text{ s}^{-1}$	[1]
K_2	$10^{-10.32} \text{ mol L}^{-1}$	[1]	k_{2r}	k_{2f}/K_1	[1]
K_w	$10^{-14} \text{ mol}^2 \text{ L}^{-2}$	[1]	k_{3f}	k_{3r}/K_4	[1]
K_3	K_1/K_w	[1]	k_{3r}	$6.0 \times 10^9 \text{ L mol}^{-1} \text{ s}^{-1}$	[1]
K_4	K_2/K_w	[1]	k_{4f}	k_{4r}/K_2	[1]
k_{1f}	$8.42 \times 10^3 \text{ L mol}^{-1} \text{ s}^{-1}$	[3]	k_{4r}	59.44 s^{-1}	[1]
k_{1r}	k_{1f}/K_3	[1]	k_{5f}	$2.3 \times 10^{10} \text{ L mol}^{-1} \text{ s}^{-1}$	[4]
			k_{5r}	$K_w k_{4f}$	[1]

Table S3: Table of Sechenov coefficients, used in the surface reaction modeling for Ag.

Sechenov constant	Value ($\text{m}^3 \text{mol}^{-1}$)	Ref.
h_{g,CO_2}	-1.7159×10^{-5}	[5]
h_{s,H^+}	0.0	[5]
h_{s,OH^-}	8.39×10^{-5}	[5]
h_{s,K^+}	9.2×10^{-5}	[5]
$h_{s,\text{CO}_3^{2-}}$	14.23×10^{-5}	[5]
h_{s,HCO_3^-}	9.67×10^{-5}	[5]

S2. Fluid flow modeling details

In flow reactor setups, the relative strengths of the dissolved species transport (i.e., mass transfer) effects versus fluid viscous effects at the catalyst surface can be quantified using the Schmidt number, which for each species k is written as $Sc_k = \nu/D_k$, with ν being the fluid solvent viscosity. Values of Sc_k are typically large ($\gg 1$) in flow reactors^[6], meaning that the concentration boundary layer of each species is much thinner than the momentum boundary layer. Thus, when modeling the near-wall flow reactor behavior, the fluid velocity can be approximated as a shear flow with constant shear rate $\dot{\gamma}$ as a simplified representation. The flow velocity is an input to the bulk chemistry through the species flux in eq. (4) of the main text; we employ a one-way coupled assumption to treat the flow velocity as being not influenced by the chemistry.

To select values of Pe , an example experimental 3D rectangular flow channel with electrode length $L_x = 2.2$ cm, width $w = 3.5$ mm, and height $h = 2$ mm is considered. The 2D shear rate of the computational domain can be analytically converted to and from the experimental flow rate of a 3D rectangular flow channel. Following Stone^[7], for a pressure-driven flow in a channel with a rectangular cross-section with flow rate Q , pressure drop Δp , and dynamic viscosity μ , the pressure gradient is given as

$$\frac{\Delta p}{L_x} = \frac{12\mu Q}{wh^3} \frac{1}{1 - 6\left(\frac{h}{w}\right) \sum_{n=0}^{\infty} \lambda_n^{-5} \tanh\left(\frac{\lambda_n w}{h}\right)}, \quad (1)$$

where $\lambda_n = (2n + 1)\pi/2$. The shear rate $\dot{\gamma}$, along the midline of the plate parallel to the flow direction, is given as

$$\dot{\gamma} = \left. \frac{\partial u}{\partial y} \right|_{\text{midline}} = \frac{\Delta p}{L_x} \frac{1}{2\mu} \left(h + \frac{2}{h} \sum_{n=0}^{\infty} a_n \lambda_n \sin(-\lambda_n) \right), \quad (2)$$

where $a_n = h^2(-1)^n / [(\lambda_n)^3 \cosh(\lambda_n w/h)]$ are the Fourier coefficients solved using the side-wall no-slip boundaries. Thus, for an experimental (3D) flow rate Q , the shear rate $\dot{\gamma}$ can be computed and then plugged into eq. (22) of the main text to obtain the Péclet number Pe needed for the computational simulation (2D) setup. This value of $\dot{\gamma}$ also determines the fluid velocity, as expressed in eq. (6) of the main text.

For this study, the conversion factor ends up as $Q = 1.0$ ml/min $\leftrightarrow Pe = 2.41 \times 10^6$.

S3. Ag surface chemistry formulation

The Tafel expressions^[8] describe the Ag surface reactions (given by eq. (10) and eq. (11) in the main text). The Tafel expressions are re-written here:

$$i_{\text{CO,local}} = \left(\frac{a_{\text{CO}_2}}{a_{\text{CO}_2}^{\text{bulk}}} \right)^{-\gamma_{\text{CO}_2,\text{CO}}} \left(\frac{a_{\text{OH}^-}}{a_{\text{OH}^-}^{\text{bulk}}} \right)^{-\gamma_{\text{OH}^-, \text{CO}}} i_{0,\text{CO}} \left(-\exp \left[-\frac{\alpha_{c,\text{CO}} F}{RT} \eta_{s,\text{CO}} \right] \right), \quad (3)$$

$$i_{\text{H}_2,\text{local}} = \left(\frac{a_{\text{OH}^-}}{a_{\text{OH}^-}^{\text{bulk}}} \right)^{-\gamma_{\text{OH}^-, \text{H}_2}} i_{0,\text{H}_2} \left(-\exp \left[-\frac{\alpha_{c,\text{H}_2} F}{RT} \eta_{s,\text{H}_2} \right] \right). \quad (4)$$

The following exponents of the activity terms are defined:

$$\gamma_{\text{CO}_2,\text{CO}} = -\frac{2 - \alpha_{c,\text{CO}}}{2}, \quad (5a)$$

$$\gamma_{\text{OH}^-, \text{CO}} = \alpha_{c,\text{CO}}, \quad (5b)$$

$$\gamma_{\text{OH}^-, \text{H}_2} = \alpha_{c,\text{H}_2}. \quad (5c)$$

and the following overpotential expressions are used:

$$\eta_{s,\text{CO}} = \phi_s - \phi_l - \left(U_{\text{CO}}^0 - \frac{2.303RT}{F} \text{pH} + \frac{RT}{2F} \ln(a_{\text{CO}_2}) \right), \quad (6a)$$

$$\eta_{s,\text{H}_2} = \phi_s - \phi_l - \left(U_{\text{H}_2}^0 - \frac{2.303RT}{F} \text{pH} \right). \quad (6b)$$

ϕ_s is the potential of the solid surface at $y = 0$, and is equal to the applied voltage U_{app} . In these expressions, the following values (as listed in Corpus et al.^[8]) of the transfer coefficient $\alpha_{c,k}$,

exchange current density $i_{0,k}$, and reference voltage U_k^0 are used:

$$\begin{aligned}
\alpha_{c,H_2} &= 0.312, \\
\log_{10} (i_{0,H_2} [\text{mA cm}^{-2}]) &= -6.77, \\
\alpha_{c,CO} &= 0.544, \\
\log_{10} (i_{0,CO} [\text{mA cm}^{-2}]) &= -6.72, \\
U_{CO}^0 &= -0.11 \text{ V versus SHE}, \\
U_{H_2}^0 &= 0.0 \text{ V versus SHE}.
\end{aligned} \tag{7}$$

The pH is defined as

$$\text{pH} = -\log_{10} (a_{H^+}), \tag{8}$$

where a_k refers to the activity of species k in the model and is calculated as

$$a_k = \frac{f_k c_k}{c_{ref}}, \tag{9}$$

where c_{ref} is a reference concentration equal to $1M$. f_k is the activity coefficient of species k . For each ionic species, f_k is calculated by the Davies activity coefficient, written as

$$f_k = 10^{-0.51z_k^2 \left(\frac{\sqrt{I}}{1+\sqrt{I}} - 0.3I \right)}, \tag{10}$$

where I is the (molar) ionic strength of the electrolyte, which is defined as

$$I = \frac{1}{2} \sum_k^N c_k z_k^2. \tag{11}$$

Note that when computing I to obtain f_k , the concentrations c_k should be given in units of mol/L = M.

For CO_2 , the activity coefficient is given using Sechenov coefficients (whose values are provided

in table S3), as

$$f_{k=\text{CO}_2} = \exp \left(\sum_k^{N_{\text{ionic}}} c_k (h_{s,k} + h_{g,\text{CO}_2}) \right), \quad (12)$$

where k on the right-hand-side refers to the index of the ionic species and N_{ionic} is the total number of ionic species.

Boundary conditions. The boundary conditions for species fluxes at the Ag/electrolyte interface ($y = 0$) are:

$$\begin{aligned} \mathbf{J}_{\text{CO}_2} \cdot \mathbf{n} &= \frac{i_{\text{CO,local}}}{2F}, \\ \mathbf{J}_{\text{OH}^-} \cdot \mathbf{n} &= -\frac{i_{\text{CO,local}} + i_{\text{H}_2,\text{local}}}{F}, \\ \mathbf{J}_{\text{all other species}} \cdot \mathbf{n} &= 0. \end{aligned} \quad (13)$$

\mathbf{n} is the outward normal vector.

S4. Ag surface chemistry validation of implementation

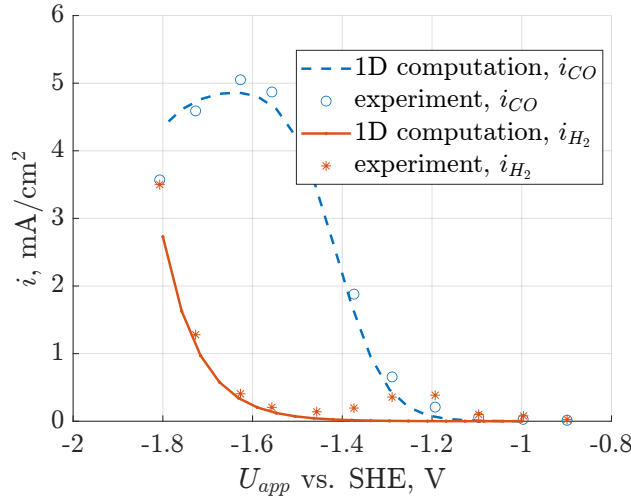


Figure S1: Comparison of 1D computations (from this current investigation) with experimental data^[9], for partial current densities (as given by the Tafel expressions in eq. (3) and eq. (4)) versus applied voltage U_{app} .

To ensure the Ag surface chemistry is correctly implemented and compares well with the reference

experimental observations, a one-dimensional (1D) computational case is run. For the computational setup, at one end the catalyst boundary Ag is set; at the other end, the same bulk concentrations are used as is for all cases run in this study (as specified in section 2.2.1 of the main text). The domain size is set by the boundary layer thickness, which is $174\text{ }\mu\text{m}$ as set by the experimental dataset used (from Clark et al.^[9], and specified as dataset 002 from Corpus et al.^[8]).

Results are shown in fig. S1. The profiles for both i_{CO} and i_{CO} match well with the experimental results, especially the behavior at more negative U_{app} values. The slight bump increase in i_{H_2} at intermediate U_{app} is not captured; this behavior has been attributed to the reduction of protons from bicarbonate^[10], which is an effect not considered in the Tafel modeling method utilized here. However, overall agreement in the trend and numerical values is acceptable and gives confidence that the important and relevant Ag surface chemistry behavior is being captured.

S5. Cu surface chemistry formulation

The Tafel expressions^[11] describe the Cu surface reactions (given by eq. (14) through eq. (17) in the main text). The Tafel expressions are re-written here:

$$i_{\text{C}_2\text{H}_4, \text{local}} = \left(\frac{c_{\text{CO}}}{c_{\text{ref}}} \right) i_{0, \text{C}_2\text{H}_4} \left(-\exp \left[-\frac{\alpha_{c, \text{C}_2\text{H}_4} F}{RT} \eta_{s, \text{C}_2\text{H}_4} \right] \right), \quad (14)$$

$$i_{\text{C}_2\text{H}_6\text{O}, \text{local}} = \left(\frac{c_{\text{CO}}}{c_{\text{ref}}} \right) i_{0, \text{C}_2\text{H}_6\text{O}} \left(-\exp \left[-\frac{\alpha_{c, \text{C}_2\text{H}_6\text{O}} F}{RT} \eta_{s, \text{C}_2\text{H}_6\text{O}} \right] \right), \quad (15)$$

$$i_{\text{CH}_4, \text{local}} = \left(\frac{c_{\text{CO}}}{c_{\text{ref}}} \right) i_{0, \text{CH}_4} \left(-\exp \left[-\frac{\alpha_{c, \text{CH}_4} F}{RT} \eta_{s, \text{CH}_4} \right] \right), \quad (16)$$

$$i_{\text{H}_2, \text{local}} = i_{0, \text{H}_2} \left(-\exp \left[-\frac{\alpha_{c, \text{H}_2} F}{RT} \eta_{s, \text{H}_2} \right] \right). \quad (17)$$

c_{ref} for eq. (14) through eq. (17) is set to a value of 1 mol/m³.

The overpotential U_k for each product species k is written as

$$\eta_{s, k} = \phi_s - \phi_l - U_k^0, \quad (18)$$

for $k = \{\text{C}_2\text{H}_4, \text{C}_2\text{H}_6\text{O}, \text{CH}_4, \text{H}_2\}$. The necessary parameters $\alpha_{c, k}$ are obtained by fitting to data provided by Li et al.^[11] (specifically the pH = 7.2 set of data), yielding the following values of the transfer coefficient $\alpha_{c, k}$ and exchange current density $i_{0, k}$:

$$\begin{aligned} \alpha_{c, \text{C}_2\text{H}_4} &= 0.4990, \\ i_{0, \text{C}_2\text{H}_4} &= 1.3835 \times 10^{-11} \text{ A m}^{-2}, \\ \alpha_{c, \text{C}_2\text{H}_6\text{O}} &= 0.4452, \\ i_{0, \text{C}_2\text{H}_6\text{O}} &= 8.9302 \times 10^{-11} \text{ A m}^{-2}, \\ \alpha_{c, \text{CH}_4} &= 0.4731, \\ i_{0, \text{CH}_4} &= 2.0064 \times 10^{-11} \text{ A m}^{-2}, \\ \alpha_{c, \text{H}_2} &= 0.4731, \\ i_{0, \text{H}_2} &= 4.627 \times 10^{-5} \text{ A m}^{-2}. \end{aligned} \quad (19)$$

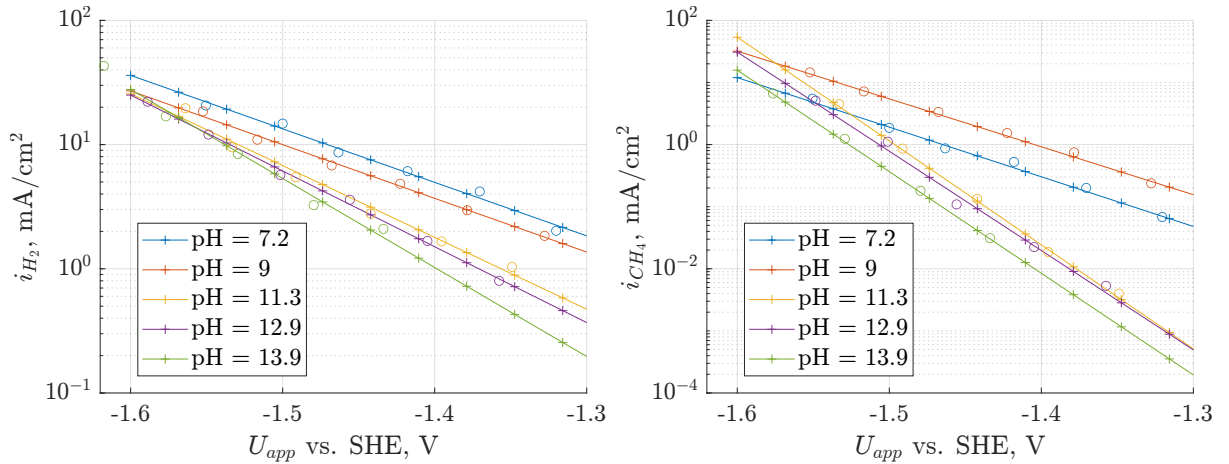
For these parameters reported here, the reference voltage $U_k^0 = 0.0\text{V}$ vs. SHE for $k = \text{C}_2\text{H}_4$, $\text{C}_2\text{H}_6\text{O}$, CH_4 , and H_2 .

Boundary conditions. The boundary conditions for species fluxes at the Cu/electrolyte interface ($y = 0$) are:

$$\begin{aligned}\mathbf{J}_{\text{CO}} \cdot \mathbf{n} &= \frac{i_{\text{C}_2\text{H}_4,\text{local}}}{4F} + \frac{i_{\text{C}_2\text{H}_6\text{O},\text{local}}}{4F} + \frac{i_{\text{CH}_4,\text{local}}}{6F}, \\ \mathbf{J}_{\text{OH}^-} \cdot \mathbf{n} &= -\frac{i_{\text{C}_2\text{H}_4,\text{local}} + i_{\text{C}_2\text{H}_6\text{O},\text{local}} + i_{\text{CH}_4,\text{local}} + i_{\text{H}_2,\text{local}}}{F}, \\ \mathbf{J}_{\text{all other species}} \cdot \mathbf{n} &= 0.\end{aligned}\tag{20}$$

\mathbf{n} is the outward normal vector.

S6. Cu surface chemistry validation



(a) H_2 (as given by the Tafel expression in eq. (17)) (b) CH_4 (as given by the Tafel expression in eq. (16))

Figure S2: Comparison of 1D computations (from this current investigation) with experimental data^[11], for partial current densities (as given by the Tafel expression in eq. (17)) versus applied voltage U_{app} . Experimental values are shown with empty circles.

To ensure the Cu surface chemistry is correctly implemented and compares well with the reference experimental observations, a one-dimensional (1D) computational case is run. The 1D computa-

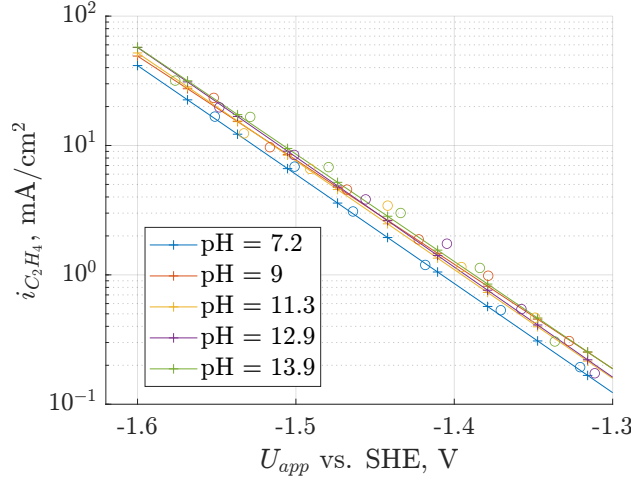


Figure S3: Comparison of 1D computations (from this current investigation) with experimental data^[11], for partial current densities (as given by the Tafel expression in eq. (14)) versus applied voltage U_{app} . Experimental values are shown with empty circles.

tional setup follows that of the 1D Ag case in section S4, with the sole difference being that the bulk CO concentration is set to 0.95 mM (corresponding to the solubility limit of CO in water at a pressure of 1 atmosphere). Each of the 5 reported pH values in Li et al.^[11] yields a different set of Tafel parameter values. Validation results for all 5 pH values are shown here in order to check the implementation; however, as discussed in section S5, only the parameters for pH = 7.2 are used in computing the results of the current study. A very thin boundary layer thickness of 0.01 μm is set to ensure the simulations exist comfortably in the mass transport-limited regime. The results for three product species – H_2 , CH_4 , C_2H_4 – are shown in fig. S2a, fig. S2b, and fig. S3. This validation exercise checks that the implemented Tafel expressions yield current density profiles that match well with the corresponding experimental values; this is indeed the case.

S7. Manually-patterned $N = 2$ cases, Faradaic Efficiency (FE)

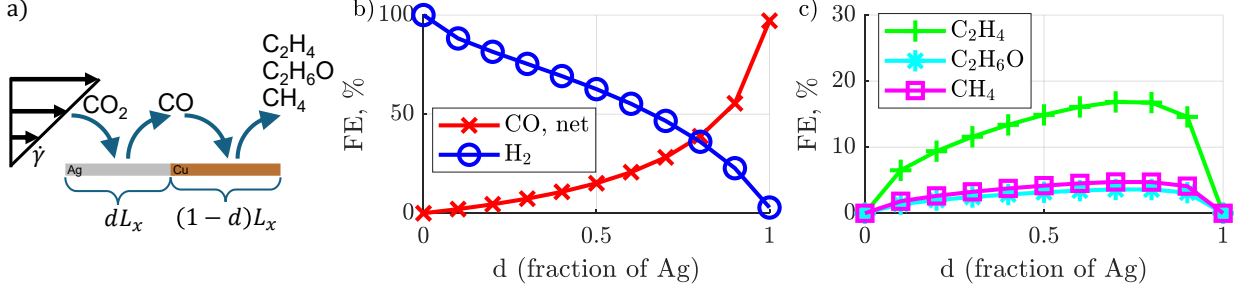


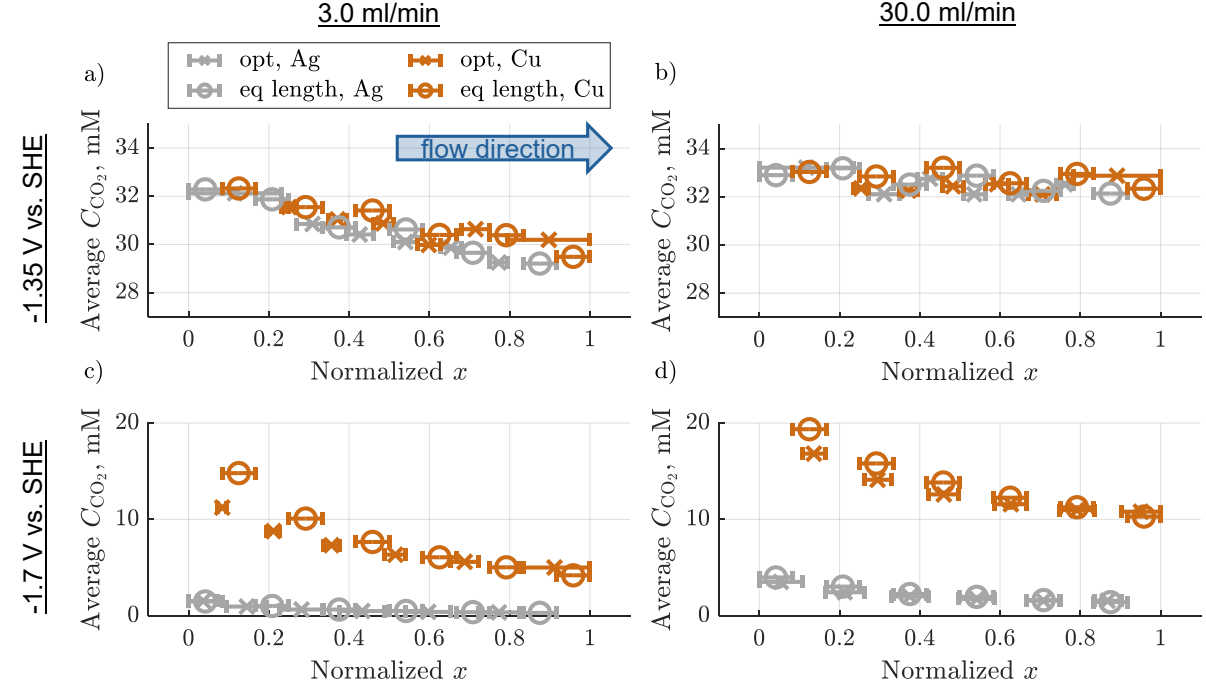
Figure S4: a) A schematic depicting the patterning configuration $N = 2$, along with the cascade reaction pathway considered: $\text{CO}_2 \longrightarrow \text{CO} \longrightarrow \{\text{C}_2\text{H}_4, \text{C}_2\text{H}_6\text{O}, \text{CH}_4\}$. d denotes the fraction of the electrode length assigned to the Ag section. b) Plots of Faradaic efficiency (FE), as a percentage, for net CO and for H_2 as a function of d . c) Plots of FE, as a percentage, for C_2H_4 , $\text{C}_2\text{H}_6\text{O}$, and CH_4 as a function of d . The cases run to obtain the current density values in b and c use the same conditions as chosen in fig. 1 of the main text: flow rate = 3.0 ml/min, $U_{app} = -1.7$ V vs. SHE.

The Faradaic efficiency (FE) for product species k is computed as

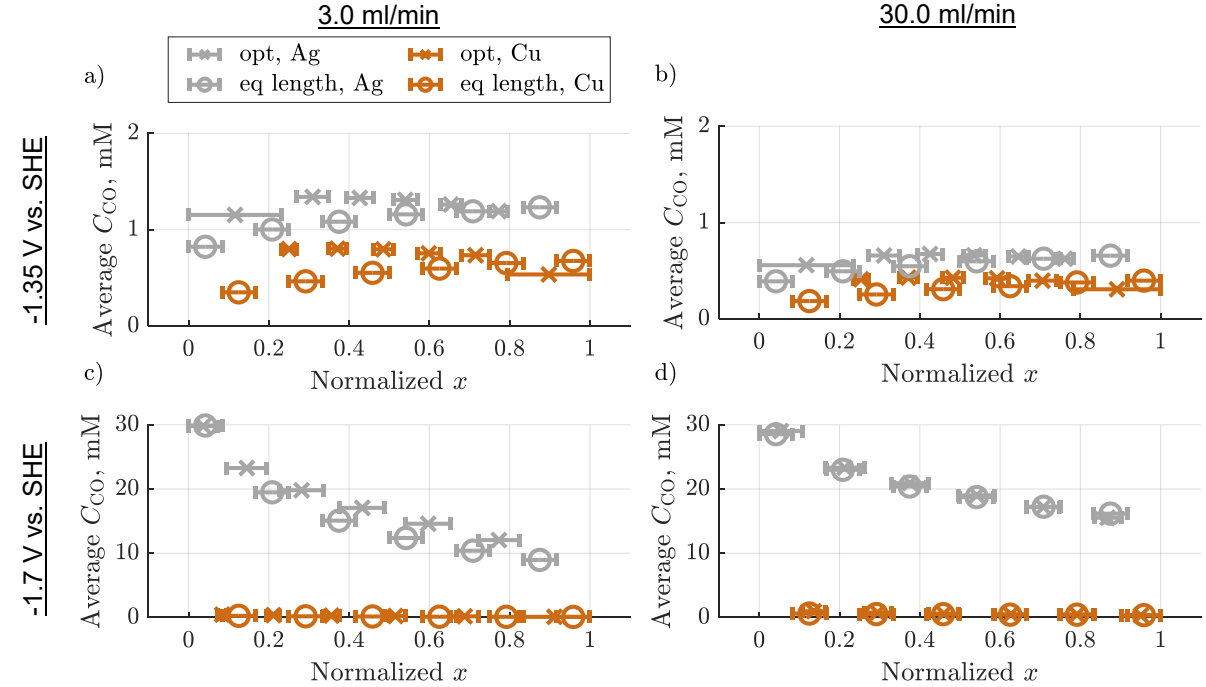
$$\text{FE}_k = \frac{i_k}{i_{\text{H}_2} + i_{\text{CO,net}} + i_{\text{C}_2\text{H}_4} + i_{\text{C}_2\text{H}_6\text{O}} + i_{\text{CH}_4}}. \quad (21)$$

In fig. S4, it is observed that a trivial optimization maximum occurs for FE of CO (at $d = 1$) and for H_2 (at $d = 0$), and a nontrivial optimization maximum occurs for FE for C_2H_4 , $\text{C}_2\text{H}_6\text{O}$, and CH_4 , just as was observed for the current density values as shown in section 3.1 of the main text. However, a key difference is that the maximum FE values for the nontrivial optimization products occur at a value of $d \simeq 0.8$, which is shifted significantly towards favoring Ag compared to the maximum at $d \simeq 0.5$ for the i values. Because the Cu kinetics used in the current study has a strong propensity towards producing H_2 , the maximum FE for the other Cu products is achieved by using configurations that use a smaller proportion of Cu to minimize the relative magnitude of the H_2 production.

S8. Average surface concentrations of CO_2 , CO , C_2H_4



(a) CO_2 plots.



(b) CO plots.

Figure S5: CO_2 and CO average surface concentrations, for $N = 12$, on each section.

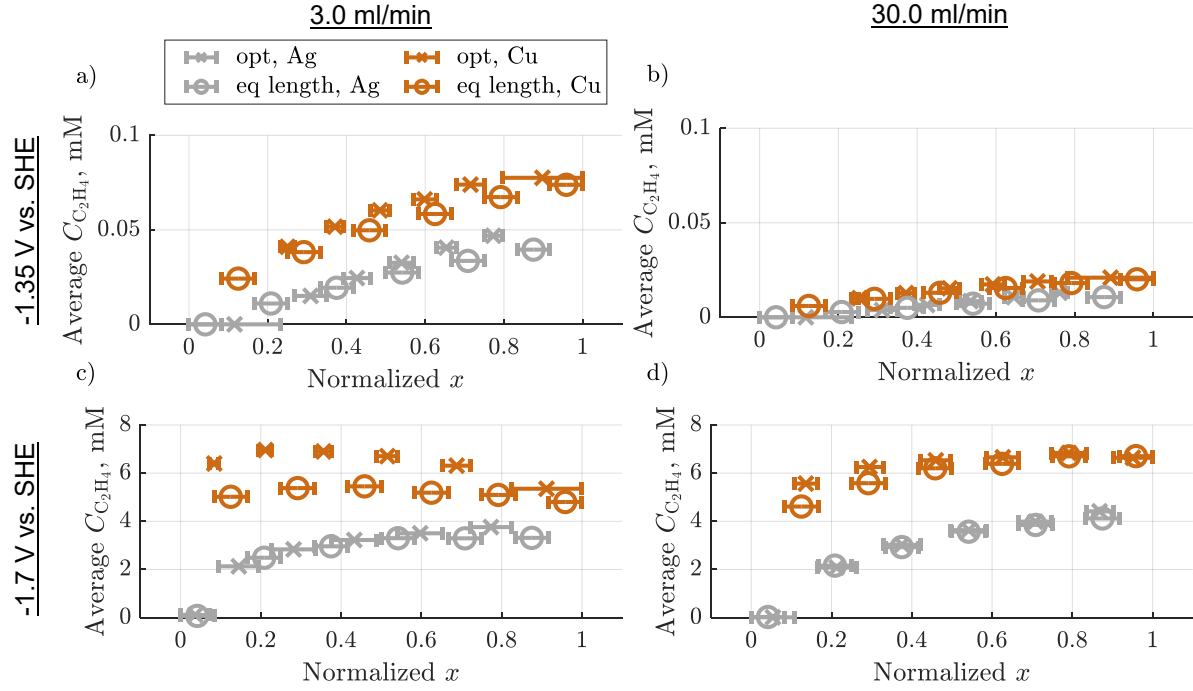


Figure S6: C_2H_4 average surface concentrations, for $N = 12$, on each section.

As discussed in the analysis for section 3.4.2 of the main text, fig. S5 and fig. S6 provide the average surface concentration of CO_2 , CO , and C_2H_4 on each of the Ag and Cu sections for the $N = 12$ equal length and optimized cases.

References

- [1] Weng, L.-C.; Bell, A. T.; Weber, A. Z. Modeling gas-diffusion electrodes for CO₂ reduction. *Physical Chemistry Chemical Physics* **2018**, *20*, 16973–16984.
- [2] Cussler, E. L. *Diffusion: mass transfer in fluid systems*; Cambridge university press, 2009.
- [3] Astarita, G.; Savage, D.; Bisio, A. Gas treating with chemical reaction. *Wiley, New York* **1983**, *213*, 817–822.
- [4] Schulz, K. G.; Riebesell, U.; Rost, B.; Thoms, S.; Zeebe, R. Determination of the rate constants for the carbon dioxide to bicarbonate inter-conversion in pH-buffered seawater systems. *Marine chemistry* **2006**, *100*, 53–65.
- [5] Zeng, J. S.; Corbin, N.; Williams, K.; Manthiram, K. Kinetic analysis on the role of bicarbonate in carbon dioxide electroreduction at immobilized cobalt phthalocyanine. *ACS Catalysis* **2020**, *10*, 4326–4336.
- [6] Lin, T. Y.; Baker, S. E.; Duoss, E. B.; Beck, V. A. Analysis of the Reactive CO₂ Surface Flux in Electrocatalytic Aqueous Flow Reactors. *Industrial & Engineering Chemistry Research* **2021**, *60*, 11824–11833.
- [7] Stone, H. A. *CMOS biotechnology*; Springer, 2007; pp 5–30.
- [8] Corpus, K. R. M.; Bui, J. C.; Limaye, A. M.; Pant, L. M.; Manthiram, K.; Weber, A. Z.; Bell, A. T. Coupling covariance matrix adaptation with continuum modeling for determination of kinetic parameters associated with electrochemical CO₂ reduction. *Joule* **2023**,
- [9] Clark, E. L.; Ringe, S.; Tang, M.; Walton, A.; Hahn, C.; Jaramillo, T. F.; Chan, K.; Bell, A. T. Influence of Atomic Surface Structure on the Activity of Ag for the Electrochemical Reduction of CO₂ to CO. *ACS catalysis* **2019**, *9*, 4006–4014.
- [10] Koshy, D. M.; Akhade, S. A.; Shugar, A.; Abiose, K.; Shi, J.; Liang, S.; Oakdale, J. S.; Weitzner, S. E.; Varley, J. B.; Duoss, E. B.; Baker, S. E.; Hahn, C.; Bao, Z.; Jaramillo, T. F.

- Chemical modifications of Ag catalyst surfaces with imidazolium ionomers modulate H₂ evolution rates during electrochemical CO₂ reduction. *Journal of the American Chemical Society* **2021**, *143*, 14712–14725.
- [11] Li, J.; Chang, X.; Zhang, H.; Malkani, A. S.; Cheng, M.-J.; Xu, B.; Lu, Q. Electrokinetic and in situ spectroscopic investigations of CO electrochemical reduction on copper. *Nature communications* **2021**, *12*, 3264.